

¹ Propagation of Pi2 Pulsations Through the Braking ² Region in Global MHD Simulations

J.B. Ream¹, R. J. Walker¹, M. Ashour-Abdalla², M. El-Alaoui², M.

Wiltberger³, M. G. Kivelson^{1,4}, M. L. Goldstein⁵

J.B. Ream, Dept. of Earth, Planetary and Space Sciences, Univ. of California, Los Angeles, 595
Charles Young Drive East, Box 951567, Los Angeles, CA, 90095-1567, USA. (jodiebt@ucla.edu)

¹Dept. of Earth, Planetary and Space

This is the author manuscript accepted for publication and has undergone full peer review but has not been through the copyediting, typesetting, pagination and proofreading process, which may lead to differences between this version and the Version of Record. Please cite this article as doi:

10.1029/2015JA021572

December 10, 2015, 5:43am

D R A F T

3 **Abstract.** We investigate the propagation of Pi2 period pulsations from
4 their origin in the plasma sheet through the braking region, the region where
5 the fast flows are slowed as they approach the inner edge of the plasma sheet.
6 Our approach is to use both the UCLA and Lyon-Fedder-Mobarry (LFM)
7 global magnetohydrodynamic (MHD) computer codes to simulate the Earth's
8 magnetosphere during a substorm that occurred on September 14, 2004 when
9 Pi2 pulsations were observed. We use two different MHD models in order to
10 test the robustness of our conclusions about Pi2. The simulations are then

Sciences, University of California, Los
Angeles, USA

²Dept. of Physics and Astronomy,
University of California, Los Angeles, USA

³High Altitude Observatory, National
Center for Atmospheric Research, Boulder,
CO, USA

⁴Dept. of Atmospheric, Oceanic and
Space Sciences, University of Michigan, Ann
Arbor, MI, USA

⁵Heliospheric Physics Laboratory,
Goddard Space Flight Center, Goddard,
MD, USA

11 compared with ground-based and satellite data. We find that the propaga-
12 tion of the pulsations in the simulations, especially through the braking re-
13 gion, depends strongly on the ionospheric models used at the inner bound-
14 ary of the MHD models. With respect to typical observed values, the mod-
15 eled conductances are high in the UCLA model and low in the LFM model.
16 The different conductances affect the flows, producing stronger line-tying that
17 slows the flow in the braking region more in the UCLA model than in the
18 LFM model. Therefore, perturbations are able to propagate much more freely
19 into the inner magnetosphere in the LFM results. However, in both models
20 Pi2 period perturbations travel with the dipolarization front (DF) that forms
21 at the earthward edge of the flow channel, but as the DF slows in the brak-
22 ing region, $-8 \leq x \leq -6 R_E$, the Pi2 period perturbations begin to travel ahead
23 of it into the inner magnetosphere. This indicates that the flow channels gen-
24 erate compressional waves with periods that fall within the Pi2 range, and
25 that, as the flows themselves are stopped in the braking region, the compres-
26 sional wave continues to propagate into the inner magnetosphere.

1. Introduction

27 ULF waves observed on the ground at substorm onset with periods between 40 and
28 150 seconds, categorized as Pi2 pulsations, have been observed and studied for over 50
29 years. Because the pulsations are observed concurrently with substorm onset they are
30 often used to determine the precise onset time and location of substorms, [e.g., *Saito*
31 *et al.*, 1976; *Sakurai and Saito*, 1976; *Olson*, 1999; *Miyashita et al.*, 2000; *Kepko et al.*,
32 2004; *Hsu and McPherron*, 2007; *Kim et al.*, 2007; *Keiling et al.*, 2008]; however, there
33 is currently no consensus on how and where the pulsations themselves are generated in
34 the magnetosphere. A recent review of Pi2 by *Keiling and Takahashi* [2011] lists seven
35 different models for Pi2 generation. The source regions described in these models range
36 from the reconnection region in the tail to the plasmasphere and each describes a different
37 mechanism for generating the pulsations.

38 In the tail models the Pi2 frequencies are inherent to the flow channel (bursty flow
39 model [*Kepko et al.*, 2001], described below), or the reconnection region itself (pulsed
40 reconnection model [*Keiling et al.*, 2006]), or they are generated by plasma instabilities in
41 the near-Earth plasma sheet (instability-driven model [*Soloviyev et al.*, 2000; *Keiling et al.*,
42 2008]). In the bursty flow model [*Kepko and Kivelson*, 1999; *Kepko et al.*, 2001, 2004],
43 bursty bulk flows (BBFs), which are plasma flows in the tail with $v_x > 100$ km/s [*An-*
44 *gelopoulos et al.*, 1992, 1994] produced by reconnection in the near-Earth plasma sheet,
45 generate Pi2 period pulsations as they travel earthward. The bursty flow model sepa-
46 rates Pi2 into three distinct categories: Transient Response (TR), Inertial Current (IC)
47 and Directly Driven (DD). As BBFs propagate earthward from the reconnection region

48 they send Alfvén waves along the field lines into the ionosphere. Due to an impedance
49 mismatch between the plasma sheet and the ionosphere, part of that signal is reflected.
50 This generates a bouncing Alfvén wave on the field lines associated with the fast flow.
51 From the ground, this bouncing Alfvén wave would be observed as Pi2 pulsations at high
52 latitudes since it is linked to the relatively distant tail. This source for Pi2 pulsations was
53 first discussed by *Southwood and Stuart* [1980] and it is included in the bursty flow model
54 as the source for TR Pi2.

55 As BBFs propagate into the braking region, and approach the inner edge of the plasma
56 sheet, the dipolarization front signature in B_z diminishes as the flow speed decreases
57 to background levels. IC Pi2 are generated by time variations in the flow velocity in the
58 braking region [*Shiokawa et al.*, 1997; *Yumoto et al.*, 1989; *Nagai et al.*, 1998; *Kepko et al.*,
59 2001]. Both TR and IC Pi2 pulsations are associated with the substorm current wedge
60 (SCW) *McPherron* [1972]. However, they have slightly different signatures on the ground.
61 Specifically, TR Pi2 have a damped sinusoidal form that continues after the driving flow
62 has stopped, and IC Pi2 have a relatively constant amplitude and are only present while
63 the flows are present. In addition, the waveforms of the IC Pi2 match the flow variations
64 in the magnetotail while the TR Pi2 waveforms do not [*Kepko and Kivelson*, 1999; *Kepko*
65 *et al.*, 2001].

66 For the disturbance generated by the flow channels to be observable on the ground at
67 mid- to low latitudes, the disturbance must continue propagating earthward from the inner
68 edge of the plasma sheet to low L-shells. In the bursty flow model, when the BBFs reach
69 the inner edge of the plasma sheet, they generate a compressional pulse that continues
70 to travel earthward into the inner magnetosphere. Trains of flow bursts generate packets

71 of compressional pulses that travel earthward, coupling to the shear wave at low L-shells
72 and are observed on the ground at mid- to low latitudes. These perturbations make up
73 the DD category of Pi2 pulsations.

74 Another model for the generation of Pi2 pulsations in the magnetotail is the instability-
75 driven model [*Solovyev et al.*, 2000; *Keiling et al.*, 2008; *Keiling*, 2012]. *Keiling* [2012]
76 specifically identifies the drifting ballooning mode in the near-Earth plasma sheet as the
77 source for Pi2 period pulsations measured on the ground. Pulsations generated through
78 this mechanism would be observed at high latitudes and could potentially coexist with
79 Pi2 generated through the transient response mechanism described above.

80 The set of models that describe Pi2 generation by mechanisms in the magnetotail ac-
81 count mainly for Pi2 pulsations observed at high latitudes on the ground. The bursty flow
82 model also includes a mechanism for the generation of mid- to low latitude Pi2 pulsations
83 via the directly driven (DD) category of Pi2. There are several additional models that
84 can account for mid- to low latitude Pi2 pulsations. Each of the models for Pi2 generation
85 in the inner magnetosphere requires that a disturbance in the tail must impact the inner
86 edge of the plasma sheet, exciting a compressional wave that travels earthward. The Pi2
87 frequencies are then selected out by some mechanism in the inner magnetosphere. Some
88 of the candidates for Pi2 selection in the inner magnetosphere are plasmasphere cavity
89 modes [*Saito and Matsushita*, 1968; *Yeoman and Orr*, 1989; *Sutcliffe and Yumoto*, 1991;
90 *Takahashi et al.*, 1992], plasmasphere virtual resonance (PVR) [*Fujita et al.*, 2002], and
91 plasmopause surface waves [*Chen and Hasegawa*, 1974; *Sutcliffe*, 1975; *Southwood and*
92 *Stuart*, 1980]. The difference between these models and the bursty flow model is the
93 source of the Pi2 period in the magnetic pulsations. The bursty flow model attributes the

94 period of the pulsations directly to the flow bursts while the inner magnetosphere models
95 attribute the period to wave modes associated with the plasmasphere. Observations of
96 Pi2 by *Uozumi et al.* [2009] verify the existence of shear waves that are generated by a
97 compressional wave in agreement with the directly driven model for generation of mid to
98 low latitude Pi2.

99 Each of the existing Pi2 models is based on satellite and ground-based observations.
100 However, the short duration of Pi2 packets (10-15 minutes), combined with the low spatial
101 and temporal resolution of measurements both on the ground and in the magnetotail make
102 it very difficult to understand Pi2 generation based on measurements alone. Few simula-
103 tion studies have been carried out to investigate Pi2 generation. *Lee and Lysak* [1999] used
104 an MHD simulation with ideal dipole to investigate Pi2 generation in the plasmasphere as
105 a result of a compressional disturbance propagating Earthward in the magnetotail. More
106 recently, *Fujita and Tanaka* [2013] used a global MHD simulation to investigate the TR
107 and PVR generation mechanisms for Pi2. The authors of that study found that their
108 simulation results showed compressional waves generated at the inner edge of the plasma
109 sheet that would then be trapped in the inner magnetosphere, consistent with the PVR
110 mechanism for Pi2 generation. They also concluded that if the Alfvén waves were properly
111 reflected by the ionosphere the TR Pi2 would be established. A recent event study of a
112 substorm on September 14, 2004, simulated by using the UCLA 3D global magnetohy-
113 drodynamic (MHD) model [*Ream et al.*, 2013] examined whether flow bursts generate Pi2
114 period fluctuations in the tail as they travel earthward from the reconnection region. The
115 authors showed that inside $\sim 12 R_E$ the earthward velocity, magnetic field and pressure
116 all fluctuate at Pi2 frequencies when a flow channel is present. In this paper, we follow on

117 the results of *Ream et al.* [2013] and use both the Lyon-Fedder-Mobarry (LFM) and the
118 UCLA 3D global MHD simulations to further study the Pi2 pulsations observed during
119 this substorm event. We investigate how the fluctuations generated by fast flows in the
120 tail propagate through the braking region into the inner magnetosphere. We also investi-
121 gate the effects of different ionospheric models used in the simulations on the propagation
122 of the perturbations. It has been shown that convection in the tail is strongly linked to
123 the ionospheric conductance [*Coroniti and Kennel, 1973*]. If the perturbations are being
124 carried by the fast flows from the tail into the inner magnetosphere, the magnitude of
125 the ionospheric conductance should strongly affect how far earthward the perturbations
126 can propagate. The global MHD simulations that we use lack a plasmasphere so we are
127 not able to investigate models in which the plasmasphere's response is important. We
128 focus on the disturbance in the magnetotail and near-earth plasma sheet and investigate
129 whether the Pi2 period perturbations are contained within the fast flow channels or if the
130 flow channels carry a broadband signal that would have to be filtered by some additional
131 mechanism in the inner magnetosphere.

132 The paper is organized as follows: Satellite and ground-based observations for Septem-
133 ber 14, 2004 are described in Section 2. In Section 3 we describe the MHD simulations
134 and in Section 4 we compare the results from both the UCLA and LFM models to the
135 observations. In Section 5, we identify and compare the Pi2 period perturbations in the
136 simulations and discuss their relation to the ionospheric parameters and dipolarization
137 fronts. A summary of our conclusions is given in Section 6.

2. Observations

138 The substorm selected for this case study occurred on September 14, 2004. Observations
139 of this event have previously been presented by *Cao et al.* [2008, 2012] and *Ream et al.*
140 [2013], and are shown for the interval from 1700-1900 UT in Figure 1. The panels from
141 top to bottom show a) the AL index [*Davis and Sugiura, 1966*], b) B_H from the Urumqi
142 magnetometer (northwest China; 43.80° latitude, 87.70° longitude), c) δB_H filtered to
143 Pi2 frequencies, and d) Magnetic field observations from the Double Star (TC1) satellite
144 located in the plasma sheet at (-10.2, -1.6, 1.2) R_E GSM.

145 Based on the AL index (Figure 1a), there is an interval of moderate activity (AL < -200
146 nT) and variable convection that begins at \sim 1715 UT and lasts for \sim 1 hr. At \sim 1815 UT
147 AL recovers slightly before dropping again at 1827 UT. The minimum of -857 nT occurs
148 at 1844 UT.

149 At the time of substorm onset (1822 UT), the ground station is situated at \sim 0230
150 MLT. Although this station is not ideally located to observe the substorm, it is the
151 only magnetometer available for the event with high enough resolution to observe Pi2
152 pulsations. The observations have been bandpass filtered to 6-25 mHz (Figure 1c) to
153 identify the Pi2 pulsations. Fluctuations in the H component begin at \sim 1822 UT and are
154 broken up into packets. The first packet, and the one with the largest amplitude, begins
155 at 1822 UT and continues for \sim 10 minutes. The period of the pulsations is between 60
156 and 90 seconds.

157 There is a discrepancy of \sim 5 minutes between the Pi2 onset in the Urumqi magne-
158 tometer measurements (1822 UT) and the main decrease in the AL index (1827 UT).
159 This discrepancy may be due to the poor ground coverage in the MLT region where the
160 substorm was located. However, it has been shown by *Hsu et al.* [2012] that it is not

161 uncommon for Pi2 onset to precede substorm onset determined using the AL index by
162 several minutes.

163 Auroral observations from the IMAGE spacecraft (not shown) [*Mende et al.*, 2001] show
164 a full auroral oval remaining from a previous substorm which occurred at ~ 1520 UT. A
165 bright spot begins to form in the equatorward oval at ~ 1814 UT then remains stagnant
166 for several minutes before brightening further and breaking up between 1822 and 1825
167 UT. Based on the agreement between the timing for Pi2 onset and auroral breakup we
168 identify 1822 UT as substorm onset. *Cao et al.* [2012] argues that the auroral streamers
169 observed in the IMAGE satellite auroral data between ~ 1801 and ~ 1820 UT give evidence
170 of earthward flows prior to substorm onset.

171 In addition to the ground-based and auroral observations, plasma sheet observations
172 are available from the Double Star (TC1) satellite. Data from the TC1 Fluxgate Magne-
173 tometer (FGM) [*Carr et al.*, 2005] are shown in Figure 1d. The traces show B_x (black),
174 B_y (red), and B_z (green) in nT in GSM coordinates. Based on the magnetic field mea-
175 surements, the satellite is near the edge of the plasma sheet during the interval leading
176 up to onset and within the plasma sheet during the expansion and recovery phases. TC1
177 observes a DF at ~ 1825 UT that is preceded by Pi2 period fluctuations in B_z by several
178 minutes. We will come back to this point in Section 4. This suggests a link between the
179 two phenomena and is consistent with models of Pi2 generation in the tail [e.g. *Kepko*
180 *et al.*, 2001].

181 At the time of the substorm Geotail was located in the solar wind just outside the bow
182 shock at $\sim (25, 17, -2) R_E$ GSM. Solar wind measurements from Geotail, propagated to
183 the bow shock, are also shown in Figure 1. The panels show e) magnetic field [nT], f) solar

184 wind velocity v_x [km/s], g) solar wind velocity v_y and v_z [km/s], h) density [cm^3] and
185 i) temperature [eV]. Between ~ 1640 and 1720 UT B_y dominates in the solar wind. The
186 solar wind magnetic field turns southward at 1707 UT, just over an hour before substorm
187 onset. There is a northward turning just after 1830 UT, a few minutes after substorm
188 onset.

3. Simulation

189 To investigate the propagation of Pi2 pulsations, we have simulated this substorm using
190 both the LFM and the UCLA 3D global MHD models. The goal in using two models is
191 to determine whether the fluctuations observed in the simulation are an artifact of the
192 numerical methods used in the models or if they are indicative of a more general response
193 to solar wind driving that is independent of the details of the models.

194 There are several differences between the two models in both the numerical methods
195 used and in the general set-up. A detailed description of the UCLA model can be found in
196 *Raeder et al.* [1998], *El-Alaoui* [2001], and *El-Alaoui et al.* [2009]. A detailed description
197 of the LFM model can be found in *Lyon et al.* [2004].

198 One of the major differences is in the gridding. The UCLA model uses a stretched
199 Cartesian grid which is optimized to keep high spatial resolution in the plasma sheet,
200 specifically in the near-Earth region. LFM uses a non-orthogonal, stretched spherical
201 grid. Grid spacing is set up to keep resolution high in regions of interest such as the day
202 side magnetosphere, the magnetopause and the plasma sheet. The grid resolution in the
203 tail region between -5 and $-20 R_E$ is ~ 0.17 to $0.30 R_E$ in both models for the simulations
204 used in this investigation.

205 Additionally, the treatment of the boundary conditions differs between the two models.
206 For the inner boundary, both simulations include ionospheric conductance models based
207 on the formula presented by *Robinson et al.* [1987], which accounts ionization arising from
208 both solar EUV and auroral precipitation to solve for the Hall and Pedersen conductances
209 in the ionosphere. However, the auroral contribution is calculated differently in each of
210 the models. To account for the discrete auroral contribution to the conductance, the
211 UCLA model uses the precipitation model proposed by *Knight* [1973] and *Lyons et al.*
212 [1979] to calculate the energy and energy flux of precipitating electrons that have been
213 accelerated by a parallel potential drop [see also *Fridman and Lemaire*, 1980]. The model
214 assumes steady state and incorporates precipitation only in regions of upward field-aligned
215 currents. To account for the diffuse auroral contribution, following *Kennel and Petschek*
216 [1966], the ionospheric model used in the UCLA simulation assumes that the electron
217 distributions become isotropic at a radial distance of $3.7 R_E$.

218 The ionospheric model used in LFM has been described in detail in *Fedder et al.* [1995]
219 and *Wiltberger et al.* [2009] so we only give a brief description here. The model calculates
220 the number flux and mean energy of the precipitating electrons by first calculating the
221 initial energy and thermal flux using the sound speed and the plasma density at the inner
222 boundary of the MHD region in the simulation. Constants are used in the equations
223 for number flux and mean energy to scale the precipitation energy to reasonable values
224 in order to obtain results for the conductances that are consistent with measurements
225 [*Slinker et al.*, 1999]. Next, following work by *Chiu and Cornwall* [1980] and *Chiu et al.*
226 [1981], the parallel potential drop along field lines between the inner boundary of the
227 simulation grid and the ionosphere is calculated. A scaling factor is used in this step to

228 include an effective resistivity to the field-aligned currents that is taken to be 5 times
229 larger for upward current than for downward current. This accounts for the stronger
230 electric field required to draw ‘hot’ electrons from the magnetosphere into the ionosphere
231 than that required to draw ‘cold’ electrons out of the ionosphere. Finally, the effects of
232 the field-aligned potential on the electron flux in a geomagnetic mirror field are accounted
233 for based on work by *Owens and Fedder* [1978].

234 The sunward outer boundary in the simulations is set by using solar wind observations
235 from Geotail (Figure 1e-i). In both simulations the solar wind magnetic field propagates
236 as a plane wave from the sunward boundary. Since the magnetic field is divergence-free,
237 the normal component of the solar wind magnetic field, B_n , is set to a constant in both
238 models. The UCLA model uses a minimum variance technique to identify B_n , which is
239 then set to a constant for the entire simulation interval [*El-Alaoui*, 2001]. The LFM model
240 assumes that $B_{x_SM} = 0$.

241 To ensure that we have a uniform time base for comparison between the simulations
242 and the observations, we line up the times when the northward turning in the solar wind
243 reaches the bow shock position ($12.5 R_E$). The northward turning occurs at 1832 UT in
244 the observations. Lining up the structure in the simulations resulted in a temporal shift
245 of 4 minutes in the UCLA results, and 18 minutes in the LFM. These time shifts ensure
246 that features discussed in the simulations and satellite observations have the same solar
247 wind driver. Throughout this paper we will discuss the simulation results based on the
248 timing relative to the observations.

4. Simulation Results

249 Cross-field flows are fastest near the center of the plasma sheet. In order to identify
 250 the perturbations associated with the fast flows, we must first determine the location of
 251 the plasma sheet in the simulation results. We identify the plasma sheet by selecting
 252 the surface of minimum $|B_x|$ in GSM coordinates. Since the UCLA model is set up on a
 253 Cartesian grid we simply select the z location for each (x, y) pair that has the minimum
 254 $|B_x|$ value in the region $|z| < 8 R_E$. Due to the nature of the grid in the LFM model we
 255 cannot use the same technique to identify the plasma sheet as was used for the UCLA
 256 model. Instead, we select the grid points that have $|B_x| < 2.5$ nT and $4 > z > -8 R_E$.
 257 The selected points are then projected onto a plane and linear interpolation is used to plot
 258 them on a regular grid with a grid spacing of $0.2 R_E$ in both the x and y directions. The
 259 average z value is found for each point on the grid to determine the location of the plasma
 260 sheet. In the simulation results the plasma sheet is displaced from the geomagnetic equator
 261 by several R_E at distances greater than $15 R_E$ down tail. The large span in z included in
 262 the selection criterion accounts for that displacement and allows for identification of the
 263 plasma sheet as far tailward as $-40 R_E$. We find that, in both simulations, the plasma
 264 sheet is located between $z = 2$ and $z = 0 R_E$ in the region $-12 \leq x \leq 0 R_E$ then begins
 265 to tilt in the $-z$ direction so it is located at $z \approx -7 R_E$ at $x = -30 R_E$.

266 Snapshots of the plasma properties at the location of the plasma sheet from the simu-
 267 lations are shown in Figure 2. The top panels show results from the UCLA model, and
 268 the bottom panels show results from the LFM model, every minute between 1821 and
 269 1826 UT. The background color shows B_z between 50 and -50 nT. The green color marks
 270 $-0.15 \leq B_z \leq 0.15$ nT to show approximate locations for the reconnection regions in
 271 the plasma sheet. Black arrows show the velocity in the plane and gray contours show

272 thermal pressure. In most cases there is a stagnation point in the flows at or near the
273 green regions where $B_z = 0$ supporting the assumption that reconnection is occurring in
274 those regions.

275 There are several similarities in the global configurations in the two simulations.
276 Through most of the substorm interval, the reconnecting regions (green in Figure 2)
277 in both simulations are located between -20 and -25 R_E . Reconnection in the UCLA
278 results is more patchy than in LFM, probably because the current-dependent anomalous
279 resistivity in the UCLA model allows for reconnection in more localized regions. Most of
280 the fast flows from the reconnection regions in both models are slowed and diverted before
281 reaching -12 R_E . As a result of this diversion, the flow channels that penetrate further
282 earthward are pinched into azimuthally thin structures, in agreement with observations
283 of narrow channels of fast plasma flows in the tail. The diversion itself is due to vortic-
284 ity from earlier flow channels and the formation of a secondary minimum in B_z 2-5 R_E
285 earthward of the reconnecting regions. The vorticity observed in the simulation results is
286 similar to that presented in previous MHD studies of flow channels [e.g., *El-Alaoui et al.*,
287 2009; *Birn et al.*, 2011; *El-Alaoui et al.*, 2013]. An example of the secondary minimum
288 in B_z can be found in the 1821 UT snapshots in Figure 2 at the locations marked by the
289 light blue triangles.

290 The flow channel in the UCLA results that agrees in timing and location with the ap-
291 pearance of dipolarization at the TC1 spacecraft is fairly isolated and forms near midnight
292 (0045 MLT). There are other DFs that form around the same time as the DF that agrees
293 with the TC1 observations, but they are located at different local times so they would
294 not have been observed by TC1. The flow channel in the LFM results is also located

295 very close to midnight between 0045 and 0100 MLT, but there is also a very strong flow
296 channel that forms earlier, just after 1800 UT, and persists for over 20 minutes just to
297 the dusk side of midnight between 2300 MLT and midnight. Thus, the LFM flow channel
298 that agrees with the TC1 observations is not as isolated, spatially or temporally, as is the
299 corresponding flow channel in the UCLA simulation. The dark green x in each panel of
300 Figure 2 marks the location of TC1 and the large dark blue arrows mark the earthward
301 edge of the flow channel that corresponds to the observations. The flow channels that
302 correspond to the Double Star observations in each simulation occur at similar times,
303 reaching $-8 R_E$ at ~ 1826 UT, close to the time of substorm onset. Both simulations did a
304 reasonable job reproducing DFs at the location of the TC1 observations. However, with
305 the sparse observations available for this event it is difficult to determine how localized
306 the DF was for this event, so we cannot determine whether one simulation or the other
307 more accurately recreated the DF. In general, the DFs in the UCLA model look more like
308 the medium scale flows presented by *Henderson* [2012].

309 To study the changes in the plasma sheet leading up to substorm onset in the simulations
310 we have taken snapshots at each time step and subtracted values of the parameters at
311 the previous time step ($\delta t = 30$ s). Figure 3 shows the results of the differencing for the
312 snapshots shown in Figure 2. The background color is δB_z and the arrows show δv in the
313 plane. The gray contours show the total thermal pressure giving us a reference for where
314 the DF has formed in the simulation. The DF appears as an enhancement in δB_z that is
315 both preceded and followed by a depression in δB_z . This structure is accompanied by an
316 enhancement in the earthward flow.

317 By plotting the perturbations in the plasma sheet in this manner we can see that the
318 flow channel and associated DF that forms in the UCLA results is a very well defined
319 structure that forms near $20 R_E$ and travels earthward, reaching $\sim 8 R_E$ at 1826 UT. We
320 can also see that the flow channel that formed in the LFM simulation around 1800 UT
321 is relatively steady. There is a set of DFs that form in the LFM simulation and travel
322 earthward with the flow early on, but after ~ 1815 UT there is relatively little change
323 associated with the flow channel until 1820 UT when the flow channel widens and a new
324 DF forms. As was noted above, this new DF is in the correct location to account for the
325 observations from the Double Star (TC1) satellite in the plasma sheet and the available
326 ground-based magnetometer. The green crosses and large blue arrows are the same as
327 those found in Figure 2 and mark the TC1 location and closest approach of the observed
328 DF to Earth at each timestep. A movie of the simulated plasma sheet (UCLA top left,
329 LFM top right) and the time differenced plasma sheet (UCLA bottom left, LFM bottom
330 right) for the event is included in the supplemental material. The panels in the movie
331 frames are laid out in the same format as the panels in Figures 2 and 3. The series
332 of events that occur during the course of the simulation interval are similar in the two
333 models. Reconnection begins between 1715 and 1720 UT and several flow channels form
334 and travel earthward during the hour leading up to the substorm. Most of the activity
335 prior to the substorm onset occurs in the dusk sector. At ~ 1820 UT, a flow channel
336 with an associated DF forms and crosses the TC1 location. Several additional DFs form
337 and travel earthward until ~ 1845 UT when the reconnection regions move tailward and
338 activity in the near-Earth plasma sheet diminishes.

339 Figure 4 shows δB_z , filtered to Pi2 frequencies from a) the UCLA model, and b) the LFM
340 model at the location of the Double Star (TC1) satellite, and c) Double Star observations,
341 along with d) ground Pi2 signatures (δH). In each data set there is a DF accompanied by
342 Pi2 period perturbations. The large peak at 1825 UT in the TC1 δB_z corresponds to the
343 DF in the observations, however, as was noted in Section 2, smaller amplitude Pi2 period
344 pulsations begin at ~ 1820 UT, 5 minutes before the DF arrives. In the UCLA trace (panel
345 a) perturbations begin at nearly the same time as the perturbations observed by TC1 and
346 correspond to the DF indicated by the thick arrows in the top panels of Figures 2 and 3.
347 In the LFM trace (panel b) there are perturbations beginning 1753 UT which are related
348 to the earlier, persistent, flow channel in the dusk sector. These perturbations damp out
349 by ~ 1815 , then a new packet forms at ~ 1823 UT. It is the second packet that agrees most
350 closely in time and location with the available observations. There are also perturbations
351 that begin around 1730 UT and just after 1750 UT in the UCLA simulation but the
352 responsible flow channels are a very transient structures and the perturbations damp out
353 quickly, whereas the flow channel in the LFM simulation is a persistent structure, as
354 mentioned above, that continues to drive perturbations for more than 20 minutes.

355 Although there are some obvious differences in the two simulations, each individual
356 simulation can account for the observations available during the event. The Urumqi
357 magnetometer was located at ~ 0300 MLT during the expansion phase of the substorm.
358 In the simulations and observations available for this event the flow channel locations
359 are within 2.5 hours of the Urumqi local time. Using a selection of 48 Pi2 events that
360 occurred when THEMIS was in the inner magnetosphere, *Kwon et al.* [2012] has shown
361 that space and ground observations of Pi2 are coherent if the satellite is within about

362 3 hours of MLT of the ground station. *Ream et al.* [2013] showed that the pulsations
363 observed in the UCLA simulation are coherent for ~ 2.5 hours MLT at a radial distance of
364 $6 R_E$, in good agreement with the observational results. The upper limit of the coherence
365 in the LFM results is 2 hours MLT. Therefore, it is reasonable to assume that the flow
366 channel observed by TC1 and the corresponding flow channels in the simulations would
367 contribute to the fluctuations observed by the Urumqi magnetometer beginning at ~ 1822
368 UT. Although there are several flow channels that form in each of the two simulations
369 during the substorm interval, we focus on the flow channel located closest to midnight
370 since that structure can account for the observations available for this event. The timing
371 for the TC1 DF also indicates that it is related to substorm onset.

372 The changing properties of the ionosphere in the two simulations are shown in Figure
373 5 for 1818 UT (disturbed interval prior to onset), 1828 UT (substorm onset), and 1838
374 UT (recovery phase). In general, the magnitudes of the Hall and Pedersen conductances
375 are much higher in the UCLA simulation than in the LFM simulation. As a result the
376 potential is much lower in the UCLA simulation than in the LFM simulation. However,
377 the configuration and strength of the field-aligned currents are very similar in the two
378 models throughout the growth and expansion phases of the substorm.

379 Large differences in the ionospheric conductance and potential can have a dramatic
380 effect on flow patterns in the plasma sheet. If the conductance in the ionosphere becomes
381 too large, the flows in the tail are slowed or stopped because the field-aligned currents
382 are insufficient to support the full solar wind potential drop across the polar cap and the
383 ionosphere is unable to return the magnetic flux to the day side [*Coroniti and Kennel,*
384 1973; *Walker et al.*, 2006]. Therefore, the high conductances in the UCLA model result

385 in very small flow velocities in the near-earth plasma sheet, earthward of $\sim 8 R_E$. In
386 contrast, the low conductances in the LFM results allow the plasma flows to move more
387 freely into the inner magnetosphere. This effect can be seen in Figure 2. Comparison of
388 the flow vectors between UCLA and LFM shows that the flow speeds in LFM are typically
389 higher than those in the UCLA results, particularly in the fast flow channels and in the
390 flow moving around Earth toward the dayside. Figure 2 also shows that in the region
391 $7 < r < 10 R_E$ the velocity in the flow channels in the UCLA results drops to < 50 km/s
392 while in the LFM results the velocity in the flow channels is > 100 km/s and only drops
393 below 50 km/s inside of $\sim 6.5 R_E$. In the LFM results, the flow braking region is more
394 smeared out in radial distance and the inner edge is located closer to Earth than in the
395 UCLA results.

396 Figure 6 shows field line traces taken from latitudes of -80° to -60° at 0100 MLT for
397 1) UCLA and 2) LFM. Panels a and b show the Pedersen conductance and the field-
398 aligned currents for the respective simulations at 1828 UT, just after substorm onset.
399 The numbered locations in each plot show where the foot points of the field line traces
400 are located in the ionosphere. The top row in panels c, d, and e show the field lines in
401 $x - z$ with v_x at $y=0$ plotted in color. Red shows velocity in the positive x direction and
402 blue shows velocity in the negative x direction. The bottom row shows the same field
403 lines in $x - y$ with B_z in color (red - positive, blue - negative). Panels 1c and 2c show
404 a snapshot at 1818 UT during the disturbed interval prior to substorm onset. Panels 1d
405 and 2d show a snapshot at 1828 UT, about 1 minute after onset during the expansion
406 phase. Finally, Panels 1e and 2e show a snapshot at 1838 UT which is in the recovery
407 phase of the substorm.

408 Although both simulations show plasma sheet thinning, in general, the plasma sheet is
409 thicker in the LFM model than in the UCLA model, which may be due to the resistivity
410 being purely numerical in LFM while UCLA includes an anomalous resistivity term in
411 Ohm's law. The field lines in the UCLA model are more stretched than those in the LFM
412 results for latitudes $> 65^\circ$. Additionally, the field lines become open between 70° and 75°
413 latitude in the UCLA model. In the LFM model field lines become open between 75° and
414 80° latitude. Figure 6 shows that in both simulations the field lines are dragged duskward
415 at radial distances greater than $\sim 6 R_E$. The same is true when we map field lines from
416 the local time of Urumqi into the plasma sheet. We find that they are dragged toward
417 midnight in the plasma sheet with the displacement becoming larger at higher latitudes.
418 Therefore, even though the substorm is occurring near midnight the field lines map from
419 a local time at the equator to an ionospheric location further into the dawn sector, close
420 to the Urumqi location.

421 To look at the fluctuations associated with the flow channels observed in the simulations
422 in association with substorm onset, we first identified the path of the flows in each of the
423 simulations by selecting the points in the simulation where the flows exceeded 250 km/s
424 in the interval during which the flow was observed. We then calculated the average y
425 location for each x location in that region to find the average center of the flow channel
426 as it propagated earthward. This effectively traces the path of the flow channel marked
427 by the large blue arrows in Figures 2 and 3. To identify the fluctuations in magnetic field
428 (radial and azimuthal components), velocity and pressure in the flow channel, we averaged
429 across 15 minutes of MLT on the dawn half of the flow channel at fixed radial distances
430 and plotted the results as a function of radial distance and time. Only the dawn half of

431 the flow channel was selected because the fluctuations in δB_ϕ are ideally anti-symmetric
432 about the center of the flow channel.

433 The magnetic field and velocity fluctuations for the interval 1700-1800 UT in the region
434 5-15 R_E are plotted in Figure 7. The columns show a) B_z , b) B_ϕ and c) $|v|$ for UCLA (top)
435 and LFM (bottom). B_z and $|v|$ were taken at the center of the plasma sheet while B_ϕ was
436 taken 1.5 R_E above the center of the plasma sheet. Color plots show the total value for
437 each of the three components with the path of the DF indicated by the solid black line.
438 The path of the DF was determined by using the beginning of the enhancement in the total
439 B_z in column a). The line plots show radial cuts at 6.0, 6.5, 7.0, 7.5, and 8.0 R_E bandpass
440 filtered to 6-16 mHz (16 mHz is the Nyquist frequency for the simulation output). Red
441 arrows indicate the crossing time of the DF. There are Pi2 period perturbations in B_z , B_ϕ ,
442 and $|v|$ in both simulations, however, there is also a significant broadband signal in B_z .
443 The broadband signal is more prominent in the UCLA simulation than in LFM. With the
444 limited observations available in the tail for this event it is difficult to determine whether
445 one or the other simulation has more accurately reproduced the event itself. However,
446 in general, both models show Pi2 period perturbations associated with the flow channels
447 that form in the plasma sheet, and reproduce TC1 observations, even though the models
448 use dramatically different grids and numerical methods to solve the set of MHD equations.
449 As a result we believe that the modeled Pi2 period pulsations are inherent in the MHD
450 description of the system and are independent of the initial set-up and the numerical
451 methods used.

5. Discussion

452 By using MHD simulations to address the question of how Pi2 period perturbations
453 propagate through the near-Earth plasma sheet, we are able to get a global view of
454 the system. By using two different simulations to study the same event, we are able
455 to ascertain those features of Pi2 propagation that are robust and those that reflect
456 idiosyncrasies of the simulations themselves.

457 Throughout the magnetotail, flow velocities in the LFM simulation are typically higher
458 than those in the UCLA simulation (see Figure 2). Because the flows do not propagate
459 as far earthward in the UCLA simulation the perturbations carried by the flow channels
460 are also not able to penetrate as far into the inner magnetosphere. This effect can be
461 seen in the line plots in Figure 7. Fluctuations in the flow velocity and magnetic field
462 diminish to noise levels before reaching $6.5 R_E$ in the UCLA results while in the LFM
463 results the fluctuations are still evident at $6.0 R_E$. This is likely a result of the differences
464 in the ionospheric conductance models used in the simulations (see Section 4). Figure
465 5 shows very clearly that the magnitudes of the conductances in the UCLA model are
466 much higher than those in the LFM model. The high Pedersen conductance in the UCLA
467 simulation effectively stops the earthward flow in the tail inside of $\sim 7.5 R_E$ [*Coroniti and*
468 *Kennel, 1973; Walker et al., 2006*]. In contrast, the flow in the LFM simulation is able to
469 penetrate much further earthward; in some cases as far as $5 R_E$.

470 In order to confirm our interpretation of the effects of the different Pedersen conduc-
471 tances in the two models, we compare two additional simulations run with the same model,
472 in this case the UCLA model, with different ionospheric conductances. Only the UCLA
473 model was used in order to isolate the effects of the conductance. Both simulations were
474 driven by constant idealized solar wind conditions. Solar wind conditions were $v_x = 450$

475 km/s , $n = 10 cm^{-3}$, and $P = 20 pPa$. The IMF was set to a constant $-5 nT$ for the
476 entire 4 hour simulation interval. The only difference in the two simulations is in the
477 Pedersen conductance (Σ_P). For Run 1 $\Sigma_P = 6 S$. For Run 2 $\Sigma_P = 20 S$. The results of
478 the simulations can be seen in Figure 8. The figure shows that in Run 1 fast flow channels
479 have formed by $t=3600$ s, one hour into the simulation. Fast flows continue to form and
480 propagate earthward until $t=10800$ s. In Run 2 we also see that the flow channels form
481 in the simulation by $t=3600$ s. However, by $t=7200$ s those flows have died out and no
482 new flow channels are propagating into the near-Earth region. In general, the larger the
483 Pedersen conductance, the fewer the flow channels. Those that develop for large Σ_P stop
484 further out in the tail. Run 1, with low Σ_P gives results similar to the LFM results where
485 the Pedersen conductance stays low throughout the event and fast flows continue to form
486 and propagate into the near-Earth region well into the recovery phase. Run 2, on the
487 other hand, gives results similar to those found in the UCLA simulation for the current
488 event study. Flow channels form early on in the simulation but as the event progresses, the
489 Pedersen conductance increases and fast flows are stopped further out in the magnetotail.
490 There is also a very large gradient that forms in the magnetic field which can be seen in
491 Figure 8, Panels e and f. This is similar to the magnetic field gradient that forms in the
492 UCLA model (see Figure 2). The ionospheric results for Run 1 and Run 2 also correspond
493 to the LFM and UCLA results, respectively, for the Sept 14th event. In Run 1, with low
494 Pedersen conductance, the potential gets very large, with $\Delta\Phi$ exceeding 150 keV, similar
495 to the values seen in the LFM simulation. In Run 2, with high Pedersen conductance,
496 $\Delta\Phi$ stays well below 100 keV throughout the simulation, similar to the UCLA results
497 for Sept. 14th. Since the only difference between the two runs is the magnitude of the

498 Pedersen conductance, it is reasonable to conclude that the conductance is responsible for
499 the differences in the magnetotail dynamics. This, along with the similarities between the
500 simulations mentioned above, suggests that the Pedersen conductance is also responsible
501 for differences between the UCLA and LFM results for the current event study.

502 Figure 9 shows the magnitude of $\mathbf{v} \times \mathbf{B}$ at the location of the flow channel for UCLA
503 (top) and LFM (bottom) in the same format as the color panels in Figure 7. The flux
504 transport in the UCLA model falls to very low values between 6 and 7 R_E , near the inner
505 edge of the plasma sheet. In the LFM model the flux transport stays relatively high across
506 the inner edge of the plasma sheet. This difference in the flux transport is due primarily
507 to line-tying but the pressure gradients in the two simulations also play a role in how far
508 earthward the flows are able to penetrate. The largest pressure gradients are closer to
509 Earth in the LFM simulation than in the UCLA simulation. As a result, the flow speeds
510 decrease at larger radial distance in the UCLA model so the flow channels are not able to
511 penetrate as far earthward as those in the LFM simulation.

512 The two simulations also differ in the thickness of the plasma sheet (see Figure 6)
513 and in the size and duration of the flow channels that form in the plasma sheet (see
514 Figures 2 and 3). Given these differences, when we look at the perturbations generated
515 in the flow channels observed in the simulations near the time of substorm onset we
516 see that Pi2 period fluctuations are being generated in both simulations in the same
517 way. Perturbations in B_z develop with the flow channel, and the DF that forms at the
518 earthward edge of the flow channel. *Ream et al.* [2013] showed that once the flow channel
519 reaches $\sim 12 R_E$ the frequency of the perturbations is within the Pi2 spectrum. The
520 fact that the frequency of the perturbations increases as the flow channel propagates

521 earthward supports the Transient Response (TR) model for Pi2 generation. Pi2 period
522 fluctuations also develop in B_y in association with the vortices that form on either side
523 of the flow channel, generating field aligned currents, in support of the Inertial Current
524 (IC) mechanism for Pi2 generation that is included in the bursty flow model [Kepko *et al.*,
525 2001; Keiling *et al.*, 2009; Ream *et al.*, 2013]. Because the period for the TR fluctuations
526 depends on the Alfvén transit time, and both simulations have similar results for the
527 lengths of the field lines, density and magnetic field magnitudes tailward of $\sim -7 R_E$,
528 both simulations exhibit similar periods related to the flow channels at substorm onset in
529 that region. In the UCLA model, Earthward of $-7 R_E$ line tying damps the Earthward
530 propagation of the disturbance. However, in the LFM model the perturbations are able
531 to propagate much further Earthward, so the simulation results look very different in that
532 region. However, to verify that the mechanism for Pi2 generation in the simulation is, in
533 fact, the transient response mechanism, additional work is required. We need to model an
534 additional event where there are enough ground observations to validate the ionosphere
535 results and determine whether there are Pi2 period fluctuations in the ionosphere that
536 map to the flow channels in the plasma sheet. This work is currently underway.

537 In both simulations the braking region lies in the region $-8 > x > -6 R_E$ consistent
538 with the source region for Pi2 period compressional waves identified by Uozumi *et al.*
539 [2007]. As the flow channel and its associated DF travel through the braking region and
540 approach the inner edge of the plasma sheet the perturbations begin to travel ahead of the
541 DF. This effect is most evident in B_ϕ (Figure 7 column 2) where the separation between
542 the beginning of the perturbations and the red arrow marking the crossing time of the DF
543 gets larger as the disturbance propagates earthward. The separation of the DF and the Pi2

544 period fluctuations in the braking region supports the idea proposed by *Kepko et al.* [2001],
545 that a compressional wave traveling ahead of the DF into the inner magnetosphere could
546 generate Directly Driven (DD) Pi2 pulsations at mid- to low latitudes on the ground. As
547 the compressional wave travels earthward it couples to an Alfvén wave and is transported
548 into the ionosphere where it can be observed by magnetometers on the ground [*Uozumi*
549 *et al.*, 2009, 2011].

550 Figure 10 shows the perturbations in the pressure for the interval 1800-1900 UT for
551 a) UCLA and b) LFM. The traces show total pressure (black), thermal pressure (red),
552 and magnetic pressure (green) at 6.0, 6.5, 7.0, 7.5 and 8.0 R_E associated with the flow
553 channel identified in Figure 2. The red arrow marks the time of the DF crossing at each
554 radial distance. In both simulations, the fluctuations associated with the DF show a
555 mixed mode compressional wave with the thermal and magnetic pressure nearly out of
556 phase and significant fluctuations in the total pressure. This agrees well with observations
557 of magnetotail Pi2 by *Nakamizo and Iijima* [2003], which showed that the thermal and
558 magnetic pressure fluctuations associated with the Pi2 fluctuations were out of phase. The
559 pressure fluctuations (magnetic, thermal and total) in LFM and UCLA have the about
560 same amplitude at 7.5 and 8.0 R_E , however, at 7.0 R_E the amplitude of the pressure
561 fluctuations in LFM start to get larger while the pressure fluctuations in the UCLA
562 results do not. Pressure perturbations travel further earthward in the LFM model and
563 the oscillations become very large at radial distances smaller than 7.5 R_E . Meanwhile,
564 pressure perturbations in the UCLA model decay earthward of $\sim 7.0 R_E$. As noted above,
565 this is most likely an effect of the differences in the conductances between the two models.
566 The line-tying in the UCLA model is so strong that the flow perturbations are not able

567 to propagate earthward of $7.0 R_E$. Based on the pressure perturbations shown in Figure
568 10, the compressional wave propagates more easily into the inner magnetosphere in the
569 LFM model than in the UCLA model. However, as mentioned above, based on the line
570 plots in Figure 7, both simulations show a compressional wave traveling ahead of the DF
571 as it slows in the braking region.

6. Summary

572 We have used two different 3D global MHD models, UCLA and LFM, to model the
573 generation and propagation of Pi2 pulsations during a substorm event on September 14,
574 2004. Although we are unable to rule out plasmaspheric eigenmodes as a source for Pi2
575 pulsations observed on the ground, the simulations demonstrate that, in some cases, fast
576 flows in the plasma sheet are directly responsible for generating Pi2 pulsations. When we
577 focus on the flow channel that forms around the time of substorm onset in the simulations,
578 we observe Pi2 period perturbations inside $\sim 12 R_E$ in the magnetic field, velocity and
579 pressure propagating at the same speed as the DF at the earthward edge of the fast flow
580 until it reaches the braking region in agreement with the Transient Response model for
581 Pi2 [Southwood and Stuart, 1980; Kepko et al., 2001]. However, more work is needed
582 to verify the transient response mechanism in the simulations. Pi2 period perturbations
583 are observed in B_y in association with the vortices that form on either side of the flow
584 channel in support of the Inertial Current component of the bursty flow model. As the
585 DF approaches the inner edge of the plasma sheet and is slowed in the braking region,
586 the perturbations begin to travel ahead of it as a mixed mode compressional wave. These
587 propagating compressional waves generated by the fast flows in the braking region can

588 produce Pi2 pulsations observed on the ground as described by the bursty flow model for
589 Pi2 generation [Kepko and Kivelson, 1999; Kepko et al., 2001, 2004].

590 Although the perturbations are generated in the same way in both models, the propaga-
591 tion of the perturbations into the inner magnetosphere is greatly affected by the differences
592 in the ionospheric models in the simulations. The high Pedersen conductance (~ 25 S)
593 in the UCLA results causes the flow channels and the perturbations to stop propagating
594 earthward at $\sim 7 R_E$, whereas the perturbations in the LFM results, with its maximum
595 Pedersen conductance around 9 S, are able to propagate more easily into the inner mag-
596 netosphere.

597 **Acknowledgments.** This work was supported by NASA grant NNX09AV91G. This
598 research was also supported in part by the NASA Graduate Student Research Pro-
599 gram through Goddard Space Flight Center, grant number NNX10AM08H. M. L. Gold-
600 stein and M. Ashour-Abdalla were supported by the Magnetospheric Multiscale project
601 through an Interdisciplinary Science grant to the Goddard Space Flight Center and
602 UCLA (NASA grant NNX08AO48G at UCLA). M. El-Alaoui was supported by NSF
603 Grant AGS-1265967. M. G. Kivelson was supported by NASA grant UCB/NASA NAS
604 5-02099. M. Wiltberger was supported by NASA grant number NNX13AE39G. The Na-
605 tional Center for Atmospheric Research is sponsored by the National Science Foundation.
606 We would like to acknowledge high-performance computing support from Yellowstone
607 (ark:/85065/d7wd3xhc) provided by NCAR's Computational and Information Systems
608 Laboratory, sponsored by the National Science Foundation. Computational resources for
609 the UCLA model were provided by the Extreme Science and Engineering Discovery En-
610 vironment (XSEDE), which is supported by National Science Foundation grant number

OCI-1053575. All satellite and OMNI data were obtained through the Virtual Magneto-
spheric Observatory (VMO, <http://vmo.igpp.ucla.edu/>). We acknowledge the experiment
teams that acquired, processed and provided the OMNI-included data, and J.H. King and
N.E. Papitashvili of NASA/GSFC for creating the OMNI data set. Geotail magnetic field
data were provided by T. Nagai, JAXA in Japan. We acknowledge Prof. C. Carr and
the Double Star TC1 FGM instrument team, as well as ESA, Double Star, Center for
Space Science and Applied Research, and the Chinese Academy of Sciences for Dou-
ble Star data. We also acknowledge the World Data Center for Geomagnetism, Kyoto
(<http://wdc.kugi.kyoto-u.ac.jp/index.html>), and the Geomagnetic Network of China, for
Pi2 data. We thank Krishan Khurana, Tung-Shin Hsu and Robert J. Strangeway for
helpful discussions during the course of this research.

References

- Angelopoulos, V., W. Baumjohann, C. F. Kennel, F. V. Coroniti, M. G. Kivelson, R. Pellat,
R. J. Walker, H. Luehr, and G. Paschmann (1992), Bursty bulk flows in the inner central
plasma sheet, *J. Geophys. Res.*, *97*, 4027–4039, doi:10.1029/91JA02701.
- Angelopoulos, V., C. F. Kennel, F. V. Coroniti, R. Pellat, M. G. Kivelson, R. J. Walker,
C. T. Russell, W. Baumjohann, W. C. Feldman, and J. T. Gosling (1994), Statisti-
cal characteristics of bursty bulk flow events, *J. Geophys. Res.*, *99*, 21,257–+, doi:
10.1029/94JA01263.
- Birn, J., R. Nakamura, E. V. Panov, and M. Hesse (2011), Bursty bulk flows and dipo-
larization in MHD simulations of magnetotail reconnection, *J. Geophys. Res. -Space*,
116(A15), A01210, doi:10.1029/2010JA016083.

- 632 Cao, X., Z. Y. Pu, H. Zhang, V. M. Mishin, Z. W. Ma, M. W. Dunlop, S. Y. Fu, L. Xie,
633 C. J. Xiao, X. G. Wang, Q. G. Zong, Z. X. Liu, M. V. Kubyshkina, T. I. Pulkkinen,
634 H. U. Frey, A. Korth, M. Fraenz, E. Lucek, C. M. Carr, H. Reme, I. Dandouras, A. N.
635 Fazakerley, G. D. Reeves, R. Friedel, K. H. Glassmeier, and C. P. Escoubet (2008), Mul-
636 tispacecraft and ground-based observations of substorm timing and activations: Two
637 case studies, *J. Geophys. Res. -Space*, *113*(A12), A07S25, doi:10.1029/2007JA012761.
- 638 Cao, X., Z. Y. Pu, A. M. Du, S. Tian, X. G. Wang, C. J. Xiao, H. U. Frey, M. V.
639 Kubyshkina, V. M. Mishin, S. Y. Fu, L. Xie, and Q. G. Zong (2012), Auroral streamers
640 implication for the substorm progression on September 14, 2004, *Planet. Space Sci.*, *71*,
641 119–124, doi:10.1016/j.pss.2012.07.018.
- 642 Carr, C., P. Brown, T. L. Zhang, J. Gloag, T. Horbury, E. Lucek, W. Magnes, H. O'Brien,
643 T. Oddy, U. Auster, P. Austin, O. Aydogar, A. Balogh, W. Baumjohann, T. Beek,
644 H. Eichelberger, K.-H. Fornacon, E. Georgescu, K.-H. Glassmeier, M. Ludlam, R. Naka-
645 mura, and I. Richter (2005), The Double Star magnetic field investigation: instrument
646 design, performance and highlights of the first year's observations, *Ann. Geophys.*, *23*,
647 2713–2732, doi:10.5194/angeo-23-2713-2005.
- 648 Chen, L., and A. Hasegawa (1974), A theory of long-period magnetic pulsations:
649 2. Impulse excitation of surface eigenmode, *J. Geophys. Res.*, *79*, 1033–1037, doi:
650 10.1029/JA079i007p01033.
- 651 Chiu, Y. T., and J. M. Cornwall (1980), Electrostatic model of a quiet auroral arc, *J.*
652 *Geophys. Res.*, *85*, 543–556, doi:10.1029/JA085iA02p00543.
- 653 Chiu, Y. T., A. L. Newman, and J. M. Cornwall (1981), On the structures and map-
654 ping of auroral electrostatic potentials, *J. Geophys. Res.*, *86*, 10,029–10,037, doi:

655 10.1029/JA086iA12p10029.

656 Coroniti, F. V., and C. F. Kennel (1973), Can the ionosphere regulate magnetospheric
657 convection?, *J. Geophys. Res.*, *78*, 2837, doi:10.1029/JA078i016p02837.

658 Davis, T. N., and M. Sugiura (1966), Auroral electrojet activity index AE and its universal
659 time variations, *J. Geophys. Res.*, *71*, 785–801, doi:10.1029/JZ071i003p00785.

660 El-Alaoui, M. (2001), Current disruption during November 24, 1996, substorm, *J. Geo-*
661 *phys. Res.*, *106*, 6229–6246, doi:10.1029/1999JA000260.

662 El-Alaoui, M., M. Ashour-Abdalla, R. J. Walker, V. Perroomian, R. L. Richard, V. An-
663 gelopoulos, and A. Runov (2009), Substorm evolution as revealed by THEMIS satel-
664 lites and a global MHD simulation, *J. Geophys. Res. -Space*, *114*(A13), A08221, doi:
665 10.1029/2009JA014133.

666 El-Alaoui, M., R. L. Richard, M. Ashour-Abdalla, M. L. Goldstein, and R. J. Walker
667 (2013), Dipolarization and turbulence in the plasma sheet during a substorm: THEMIS
668 observations and global MHD simulations, *J. Geophys. Res. -Space*, *118*, 7752–7761,
669 doi:10.1002/2013JA019322.

670 Fedder, J. A., S. P. Slinker, J. G. Lyon, and R. D. Elphinstone (1995), Global numerical
671 simulation of the growth phase and the expansion onset for a substorm observed by
672 Viking, *J. Geophys. Res.*, *100*, 19,083–19,094, doi:10.1029/95JA01524.

673 Fridman, M., and J. Lemaire (1980), Relationship between auroral electrons fluxes
674 and field aligned electric potential difference, *J. Geophys. Res.*, *85*, 664–670, doi:
675 10.1029/JA085iA02p00664.

676 Fujita, S., and T. Tanaka (2013), Possible generation mechanisms of the Pi2 pulsations
677 estimated from a global MHD simulation, *Earth, Planets, and Space*, *65*, 453–461, doi:

678 10.5047/eps.2012.11.005.

679 Fujita, S., H. Nakata, M. Itonaga, A. Yoshikawa, and T. Mizuta (2002), A numerical
680 simulation of the Pi2 pulsations associated with the substorm current wedge, *Journal*
681 *of Geophysical Research (Space Physics)*, *107*, 1034, doi:10.1029/2001JA900137.

682 Henderson, M. G. (2012), Auroral Substorms, Poleward Boundary Activations, Au-
683 roral Streamers, Omega Bands, and Onset Precursor Activity, *Washington DC*
684 *American Geophysical Union Geophysical Monograph Series*, *197*, 39–54, doi:
685 10.1029/2011GM001165.

686 Hsu, T.-S., and R. L. McPherron (2007), A statistical study of the relation of Pi
687 2 and plasma flows in the tail, *J. Geophys. Res. -Space*, *112*(A11), A05209, doi:
688 10.1029/2006JA011782.

689 Hsu, T.-S., R. L. McPherron, V. Angelopoulos, Y. Ge, H. Zhang, C. Russell, X. Chu,
690 and J. Kissinger (2012), A statistical analysis of the association between fast
691 plasma flows and Pi2 pulsations, *J. Geophys. Res. -Space*, *117*(A16), A11221, doi:
692 10.1029/2012JA018173.

693 Keiling, A. (2012), Pi2 pulsations driven by ballooning instability, *J. Geophys. Res. -*
694 *Space*, *117*, A03228, doi:10.1029/2011JA017223.

695 Keiling, A., and K. Takahashi (2011), Review of Pi2 Models, *Space Sci. Rev.*, *161*, 63–148,
696 doi:10.1007/s11214-011-9818-4.

697 Keiling, A., M. Fujimoto, H. Hasegawa, F. Honary, V. Sergeev, V. S. Semenov, H. U. Frey,
698 O. Amm, H. Rème, I. Dandouras, and E. Lucek (2006), Association of Pi2 pulsations
699 and pulsed reconnection: ground and Cluster observations in the tail lobe at 16 R_E ,
700 *Ann. Geophys.*, *24*, 3433–3449, doi:10.5194/angeo-24-3433-2006.

- 701 Keiling, A., V. Angelopoulos, D. Larson, R. Lin, J. McFadden, C. Carlson, J. W. Bonnell,
702 F. S. Mozer, K.-H. Glassmeier, H. U. Auster, W. Magnes, S. Mende, H. Frey, A. Roux,
703 O. LeContel, S. Frey, T. Phan, E. Donovan, C. T. Russell, I. Mann, W. Liu, X. Li,
704 M. Fillingim, G. Parks, K. Shiokawa, and J. Raeder (2008), Correlation of substorm
705 injections, auroral modulations, and ground Pi2, *Geophys. Res. Let.*, *35*, L17S22, doi:
706 10.1029/2008GL033969.
- 707 Keiling, A., V. Angelopoulos, A. Runov, J. Weygand, S. V. Apatenkov, S. Mende, J. Mc-
708 Fadden, D. Larson, O. Amm, K.-H. Glassmeier, and H. U. Auster (2009), Substorm
709 current wedge driven by plasma flow vortices: THEMIS observations, *Journal of Geo-*
710 *physical Research (Space Physics)*, *114*, A00C22, doi:10.1029/2009JA014114.
- 711 Kennel, C. F., and H. E. Petschek (1966), Limit on Stably Trapped Particle Fluxes, *J.*
712 *Geophys. Res.*, *71*, 1.
- 713 Kepko, L., and M. Kivelson (1999), Generation of Pi2 pulsations by bursty bulk flows, *J.*
714 *Geophys. Res.*, *104*, 25,021–25,034, doi:10.1029/1999JA900361.
- 715 Kepko, L., M. G. Kivelson, and K. Yumoto (2001), Flow bursts, braking, and Pi2 pulsa-
716 tions, *J. Geophys. Res.*, *106*, 1903–1916, doi:10.1029/2000JA000158.
- 717 Kepko, L., M. G. Kivelson, R. L. McPherron, and H. E. Spence (2004), Relative tim-
718 ing of substorm onset phenomena, *J. Geophys. Res. -Space*, *109*(A18), A04203, doi:
719 10.1029/2003JA010285.
- 720 Kim, K.-H., K. Takahashi, S. Ohtani, and S.-K. Sung (2007), Statistical analysis of the
721 relationship between earthward flow bursts in the magnetotail and low-latitude Pi2
722 pulsations, *J. Geophys. Res. -Space*, *112*(A11), A10211, doi:10.1029/2007JA012521.
- 723 Knight, S. (1973), Parallel electric fields, *Planet. Space Sci.*, *21*(5), 741 – 750, doi:

- 724 [http://dx.doi.org/10.1016/0032-0633\(73\)90093-7](http://dx.doi.org/10.1016/0032-0633(73)90093-7).
- 725 Kwon, H.-J., K.-H. Kim, D.-H. Lee, K. Takahashi, V. Angelopoulos, E. Lee, H. Jin,
726 Y.-D. Park, J. Lee, P. R. Sutcliffe, and H. U. Auster (2012), Local time-dependent
727 Pi2 frequencies confirmed by simultaneous observations from THEMIS probes in the
728 inner magnetosphere and at low-latitude ground stations, *J. Geophys. Res. -Space*, *117*,
729 A01206, doi:10.1029/2011JA016815.
- 730 Lee, D.-H., and R. L. Lysak (1999), MHD waves in a three-dimensional dipolar mag-
731 netic field: A search for Pi2 pulsations, *J. Geophys. Res.*, *104*, 28,691–28,700, doi:
732 10.1029/1999JA900377.
- 733 Lyon, J. G., J. A. Fedder, and C. M. Mobarry (2004), The Lyon-Fedder-Mobarry (LFM)
734 global MHD magnetospheric simulation code, *J. Atmos. Solar-Terr. Phys.*, *66*, 1333–
735 1350, doi:10.1016/j.jastp.2004.03.020.
- 736 Lyons, L. R., D. S. Evans, and R. Lundin (1979), An observed relation between magnetic
737 field aligned electric fields and downward electron energy fluxes in the vicinity of auroral
738 forms, *J. Geophys. Res.*, *84*, 457–461, doi:10.1029/JA084iA02p00457.
- 739 McPherron, R. L. (1972), Substorm related changes in the geomagnetic tail: The growth
740 phase, *Planet. Space Sci.*, *20*, 1521, doi:10.1016/0032-0633(72)90054-2.
- 741 Mende, S. B., H. U. Frey, M. Lampton, J.-C. Gerard, B. Hubert, S. Fuselier, J. Spann,
742 R. Gladstone, and J. L. Burch (2001), Global observations of proton and electron auroras
743 in a substorm, *Geophys. Res. Lett.*, *28*, 1139–1142, doi:10.1029/2000GL012340.
- 744 Miyashita, Y., S. Machida, T. Mukai, Y. Saito, K. Tsuruda, H. Hayakawa, and P. R.
745 Sutcliffe (2000), A statistical study of variations in the near and middistant magneto-
746 tail associated with substorm onsets: GEOTAIL observations, *J. Geophys. Res.*, *105*,

- 747 15,913–15,930, doi:10.1029/1999JA000392.
- 748 Nagai, T., M. Fujimoto, R. Nakamura, Y. Saito, T. Mukai, T. Yamamoto, A. Nishida,
749 S. Kokubun, G. D. Reeves, and R. P. Lepping (1998), Geotail observations of a
750 fast tailward flow at $X_{GSM} = -15R_E$, *J. Geophys. Res.*, *103*, 23,543–23,550, doi:
751 10.1029/98JA02246.
- 752 Nakamizo, A., and T. Iijima (2003), A new perspective on magnetotail disturbances
753 in terms of inherent diamagnetic processes, *Journal of Geophysical Research (Space*
754 *Physics)*, *108*, 1286, doi:10.1029/2002JA009400.
- 755 Olson, J. V. (1999), Pi2 pulsations and substorm onsets: A review, *J. Geophys. Res.*, *104*,
756 17,499–17,520, doi:10.1029/1999JA900086.
- 757 Owens, J. H., and J. Fedder (1978), The effects of geomagnetic field aligned potential
758 differences on precipitating magnetospheric particles, *Tech. rep.*
- 759 Raeder, J., J. Berchem, and M. Ashour-Abdalla (1998), The Geospace Environment Mod-
760 eling Grand Challenge: Results from a Global Geospace Circulation Model, *J. Geophys.*
761 *Res.*, *1031*, 14,787–14,798, doi:10.1029/98JA00014.
- 762 Ream, J. B., R. J. Walker, M. Ashour-Abdalla, M. El-Alaoui, M. G. Kivelson, and M. L.
763 Goldstein (2013), Generation of Pi2 pulsations by intermittent earthward propagating
764 dipolarization fronts: An MHD case study, *J. Geophys. Res.*, *118*, 6364–6377, doi:
765 10.1002/2013JA018734.
- 766 Robinson, R. M., R. R. Vondrak, K. Miller, T. Dabbs, and D. Hardy (1987), On calcu-
767 lating ionospheric conductances from the flux and energy of precipitating electrons, *J.*
768 *Geophys. Res.*, *92*, 2565–2569, doi:10.1029/JA092iA03p02565.
- 769 Saito, T., and S. Matsushita (1968), Solar cycle effects on geomagnetic Pi 2 pulsations,

- 770 *J. Geophys. Res.*, *73*, 267, doi:10.1029/JA073i001p00267.
- 771 Saito, T., K. Yumoto, and Y. Koyama (1976), Magnetic pulsation Pi2 as a sensitive indi-
772 cator of magnetospheric substorm, *Planet. Space Sci.*, *24*, 1025–1029, doi:10.1016/0032-
773 0633(76)90120-3.
- 774 Sakurai, T., and T. Saito (1976), Magnetic pulsations Pi2 and substorm onset, *Planet.*
775 *Space Sci.*, *24*, 573–575, doi:10.1016/0032-0633(76)90135-5.
- 776 Shiokawa, K., W. Baumjohann, and G. Haerendel (1997), Braking of high-speed flows in
777 the near-Earth tail, *Geophys. Res. Let.*, *24*, 1179–1182, doi:10.1029/97GL01062.
- 778 Slinker, S. P., J. A. Fedder, B. A. Emery, K. B. Baker, D. Lummerzheim, J. G. Lyon,
779 and F. J. Rich (1999), Comparison of global MHD simulations with AMIE simula-
780 tions for the events of May 19-20, 1996, *J. Geophys. Res.*, *104*, 28,379–28,396, doi:
781 10.1029/1999JA900403.
- 782 Solovyev, S. I., D. G. Baishev, E. S. Barkova, N. E. Molochushkin, and K. Yumoto
783 (2000), Pi2 magnetic pulsations as response on spatio-temporal oscillations of auroral
784 arc current system, *J. Geophys. Res.*, *27*, 1839–1842, doi:10.1029/2000GL000037.
- 785 Southwood, D. J., and W. F. Stuart (1980), Pulsations at the substorm onset, in *Dynamics*
786 *of the Magnetosphere*, edited by S.-I. Akasofu, pp. 341–355.
- 787 Sutcliffe, P. R. (1975), The association of harmonics in Pi2 power spectra with the plasma-
788 pause, *Planet. Space Sci.*, *23*, 1581–1587, doi:10.1016/0032-0633(75)90085-9.
- 789 Sutcliffe, P. R., and K. Yumoto (1991), On the cavity mode nature of low-latitude Pi 2
790 pulsations, *J. Geophys. Res.*, *96*, 1543–1551, doi:10.1029/90JA02007.
- 791 Takahashi, K., S.-I. Ohtani, and K. Yumoto (1992), AMPTE CCE observations of Pi
792 2 pulsations in the inner magnetosphere, *Geophys. Res. Let.*, *19*, 1447–1450, doi:

- 793 10.1029/92GL01283.
- 794 Uozumi, T., H. Kawano, A. Yoshikawa, M. Itonaga, and K. Yumoto (2007), Pi 2 source
795 region in the magnetosphere deduced from CPMN data, *Planet. Space Sci.*, *55*, 849–857,
796 doi:10.1016/j.pss.2006.03.016.
- 797 Uozumi, T., S. Abe, K. Kitamura, T. Tokunaga, A. Yoshikawa, H. Kawano, R. Mar-
798 shall, R. J. Morris, B. M. Shevtsov, S. I. Solovyev, D. J. McNamara, K. Liou,
799 S. Ohtani, M. Itonaga, and K. Yumoto (2009), Propagation characteristics of Pi 2
800 pulsations observed at high- and low-latitude MAGDAS/CPMN stations: A statisti-
801 cal study, *Journal of Geophysical Research (Space Physics)*, *114*(A13), A11207, doi:
802 10.1029/2009JA014163.
- 803 Uozumi, T., K. Yumoto, T. Tokunaga, S. I. Solovyev, B. M. Shevtsov, R. Marshall,
804 K. Liou, S. Ohtani, S. Abe, A. Ikeda, K. Kitamura, A. Yoshikawa, H. Kawano, and
805 M. Itonaga (2011), AKR modulation and global Pi2 oscillation, *Journal of Geophysical
806 Research (Space Physics)*, *116*, A06214, doi:10.1029/2010JA016042.
- 807 Walker, R. J., M. Ashour-Abdalla, M. El Alaoui, and F. V. Coroniti (2006), Magneto-
808 spheric convection during prolonged intervals with southward interplanetary magnetic
809 field, *J. Geophys. Res. -Space*, *111*(A10), A10219, doi:10.1029/2005JA011541.
- 810 Wiltberger, M., R. S. Weigel, W. Lotko, and J. A. Fedder (2009), Modeling seasonal
811 variations of auroral particle precipitation in a global-scale magnetosphere-ionosphere
812 simulation, *J. Geophys. Res. -Space*, *114*, A01204, doi:10.1029/2008JA013108.
- 813 Yeoman, T. K., and D. Orr (1989), Phase and spectral power of mid-latitude Pi2 pulsations
814 - Evidence for a plasmaspheric cavity resonance, *Planet. Space Sci.*, *37*, 1367–1383, doi:
815 10.1016/0032-0633(89)90107-4.

816 Yumoto, K., T. Saito, K. Takahashi, F. W. Menk, and B. J. Fraser (1989), Some
817 aspects of the relation between Pi 1-2 magnetic pulsations observed at L = 1.3-
818 2.1 on the ground and substorm-associated magnetic field variations in the near-
819 earth magnetotail observed by AMPTE CCE, *J. Geophys. Res.*, *94*, 3611–3618, doi:
820 10.1029/JA094iA04p03611.

Author Manuscript

Figure 1. Ground and satellite observations for September 14, 2004. Panels show a) the 1 minute AL index from the OMNI database, b) B_H from the ground magnetometer in Urumqi, China, c) δB_H for the Urumqi observations filtered to Pi2 frequencies, d) Double Star (TC1) magnetic field observations in the plasma sheet, B_x (black), B_y (red), and B_z (green) in nT in GSM coordinates for the interval 1700–1900 UT. Geotail solar wind measurements in GSM coordinates for the interval 1400–1930 UT used for input in the MHD simulations are shown in panels e-f. e) Magnetic field B_x (black), B_y (red), and B_z (green) [nT], f) Solar wind velocity v_x , g) Solar wind velocity v_y (black), v_z (red) [km/s], h) density [cc^{-3}], and i) ion temperature [eV]. The dashed purple line marks the time of Pi2 onset at Urumqi. Solid purple line marks AL substorm onset. Solid blue lines mark the start and stop times for the interval shown in panels a-d. Arrows mark DF in the observations.

Figure 2. Plasma sheet results from the UCLA (top) and LFM (bottom) simulations for September 14, 2004. Snapshots are shown each minute between 1821 and 1826 UT. The area shown is $-30 \leq x \leq 0 R_E$ and $-15 \leq y \leq 15 R_E$. Background color shows B_z from -50 (blue) to 50 (red) nT with the green color marking $|B_z| < 0.15$ nT. A reference vector is shown for 500 km/s. Black arrows show the velocity in the plane and the gray contours show thermal pressure (0-4000 pPa, $\delta P = 500 pPa$). The solid black line marks the radial distance of $6 R_E$. The TC1 location is marked by the dark green x. The large blue arrow indicates the earthward edge of the DF that is consistent with TC1 observations. The blue triangle marks an example of a secondary B_z minimum a few R_E earthward of the reconnection regions. The Sun is to the right.

Figure 3. Time differenced plasma sheet results for September 14, 2004 in the same format as Figure 2. The color bar shows $-10 \leq \delta B_z \leq 10 nT$ and the reference vector shows $\delta v = 200$ km/s.

Figure 4. δB_Z bandpass filtered to 6-16 mHz for the interval 1700-1900 UT for a) UCLA, b) LFM simulations results near the TC1 location, and c) TC1 observations. The gray areas indicate times when the Pi2 in the simulation correspond to the TC1 measurements. Panel d shows the Pi2 pulsations measured from the ground for comparison (also shown in Figure 1c.)

Figure 5. Ionospheric plots for a) 1808 UT, b) 1828 UT, and c) 1848 UT. The top row in each panel shows UCLA results and the bottom row shows LFM results. Columns from left to right show Pedersen conductance [S], Hall conductance [S], Potential [kV], and parallel current [$\mu A/m^2$].

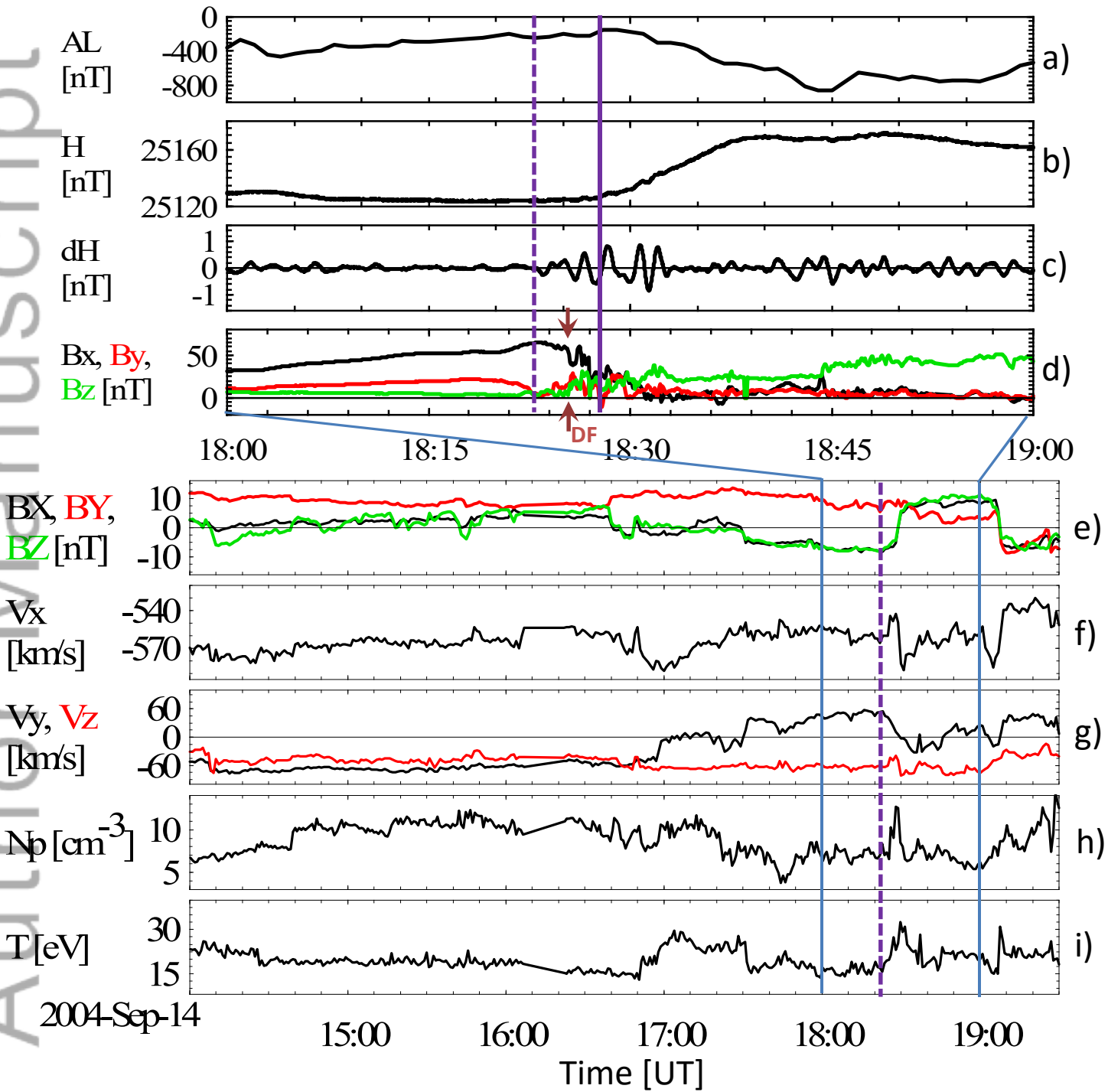
Figure 6. Results of field line traces from 1) UCLA and 2) LFM for times before, during, and after substorm onset. Panels show a) Pedersen conductance and b) parallel currents at 1828 UT. Field lines with footpoints at the numbered locations in panels a and b are shown at c) 1818 UT, d) 1828 UT, and e) 1838 UT. The top row in each panel shows an $x - z$ view of the field lines with v_x shown in the color background. The bottom row shows an $x - y$ view of the same field lines with B_z in the background. Field lines south of the geomagnetic equator are dashed. The numbers indicate which footpoint the field line corresponds to in panels a and b.

Figure 7. Average quantities and perturbations for 15 minutes of MLT on the dusk half of the flow channels that agree with the TC1 measurements as identified in Figures 2 and 3 for UCLA (above) and LFM (below) between 1700 and 1900 UT. From left to right, color plots show the average quantities B_z , B_ϕ , and $|v|$ plotted versus radial distance from Earth and time. The black line shows the path of the DF through the system determined using B_z and copied onto the other panels. The line plots show cuts between 6 and 8 R_E for each of the components bandpass filtered to 6-16 mHz (the portion of the Pi2 band that can be resolved in the simulations). Red arrows indicate the DF crossing time at each radial distance.

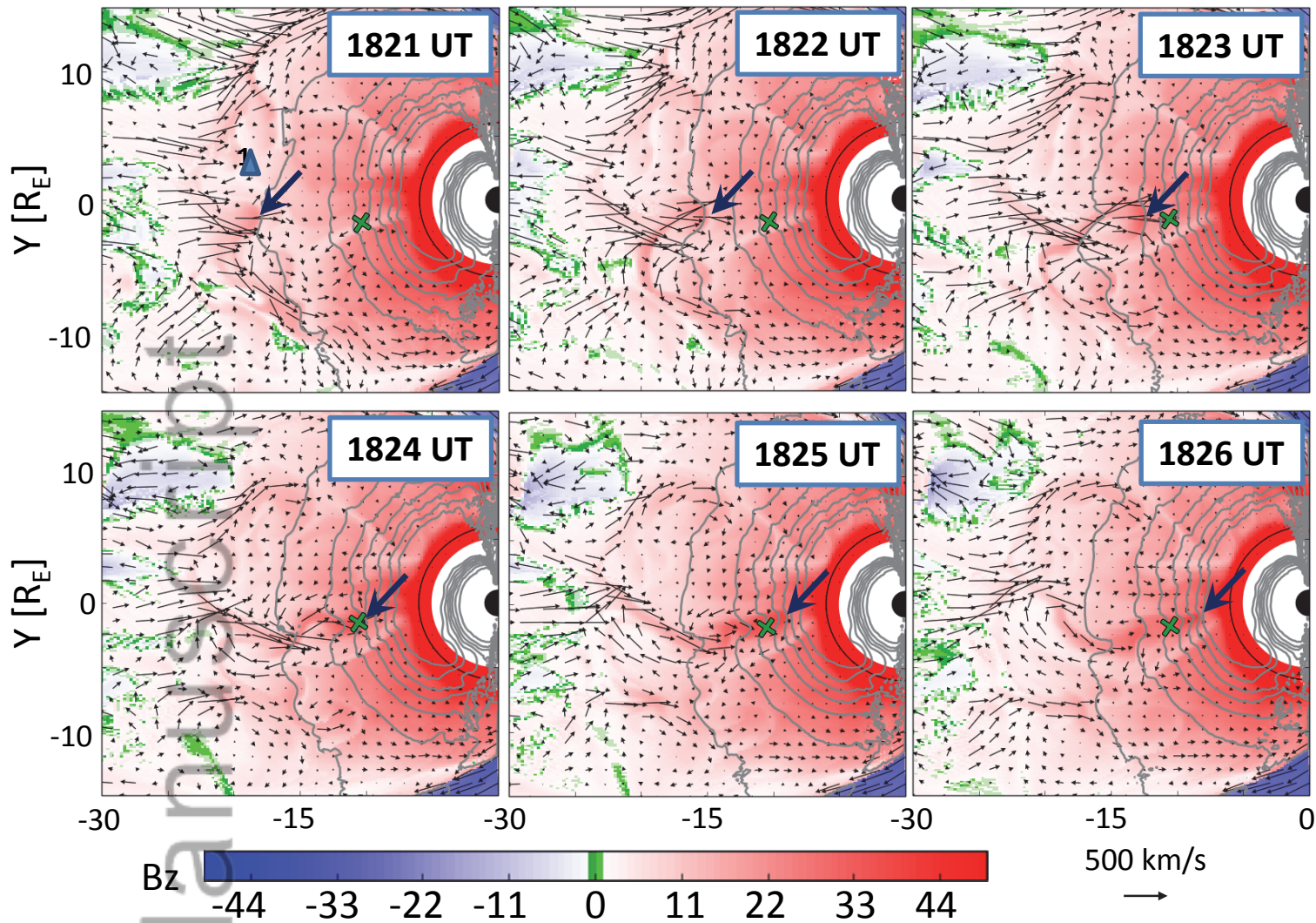
Figure 8. Simulation results from Run 1 ($\Sigma_P = 6 S$) in panels a-c, and Run 2 ($\Sigma_P = 20 S$) in panels d-f. Simulation times from left to right are $t=3600, 7200, \text{ and } 10800$ for each simulation. Background color shows B_z . Arrows show the velocity in the plane.

Figure 9. The flux transport $|\mathbf{v} \times \mathbf{B}|$ plotted in the same format as the color panels in Figure 7 for UCLA (top) and LFM (bottom).

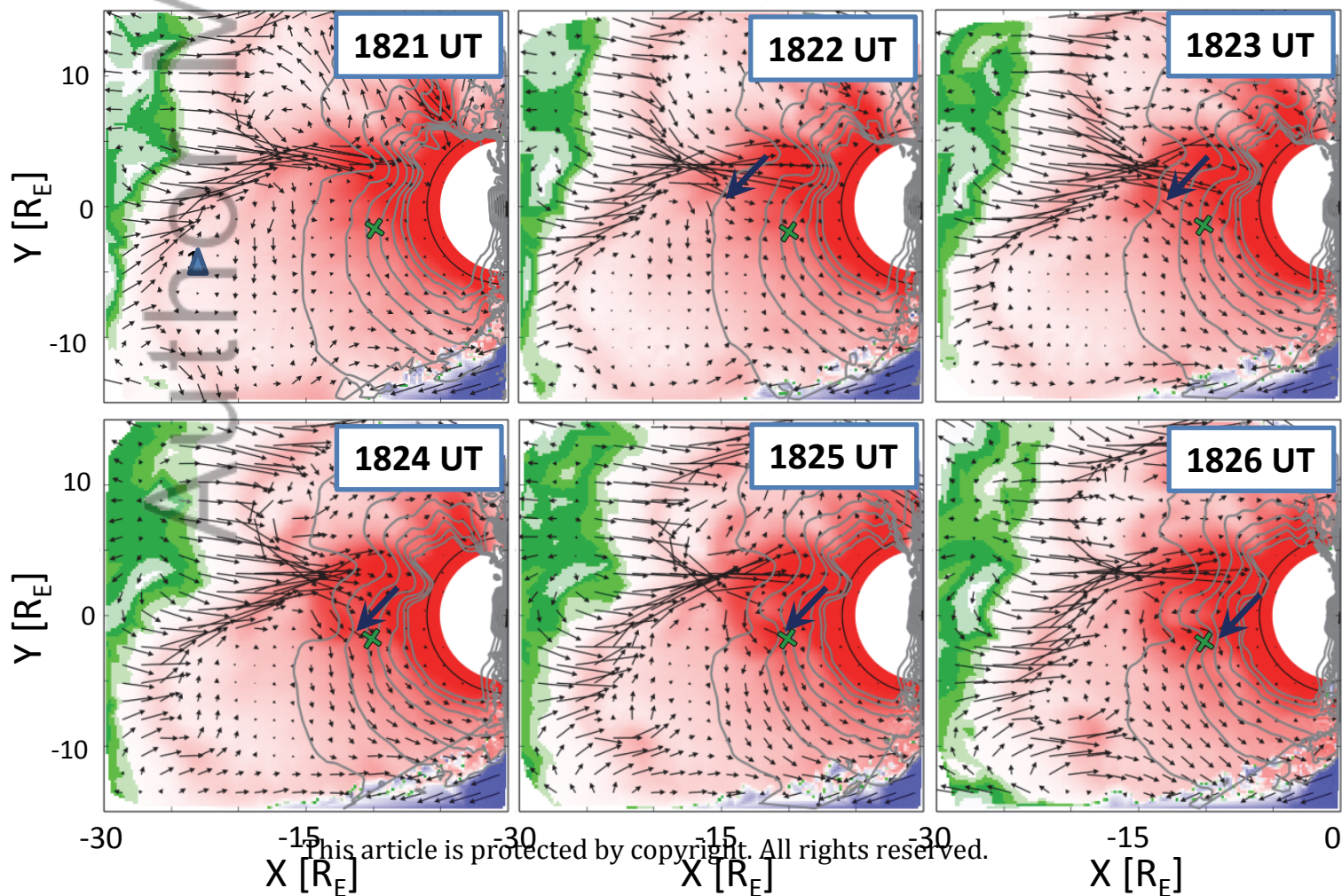
Figure 10. Pressure perturbations in the dusk half of the flow channel plotted in the same format as the line plots in Figure 7 for the interval 1800-1900 UT. Traces show δP_{total} (black), δP_{th} (red) and δP_{mag} (green) for a) UCLA and b) LFM.



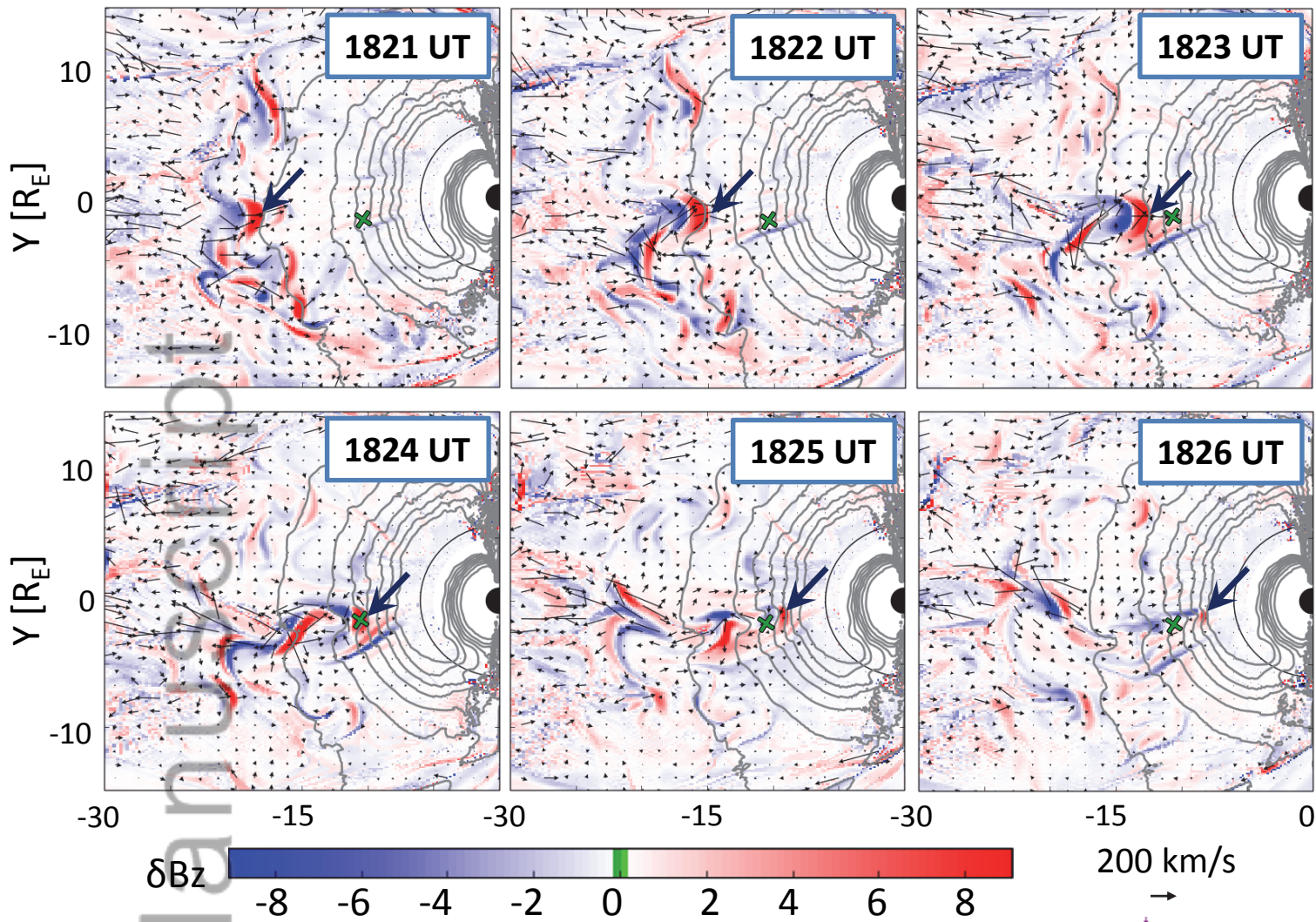
UCLA



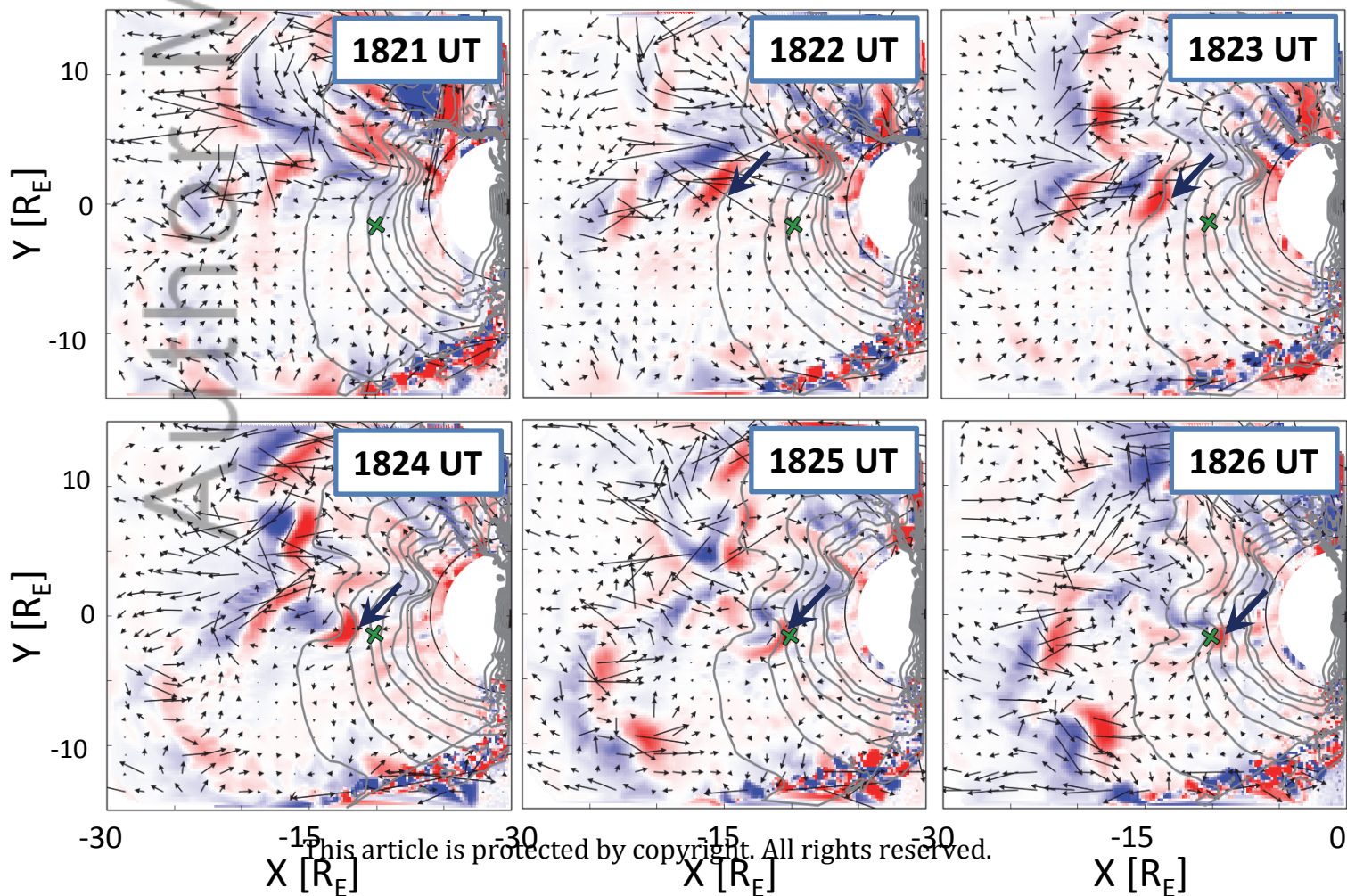
LFM

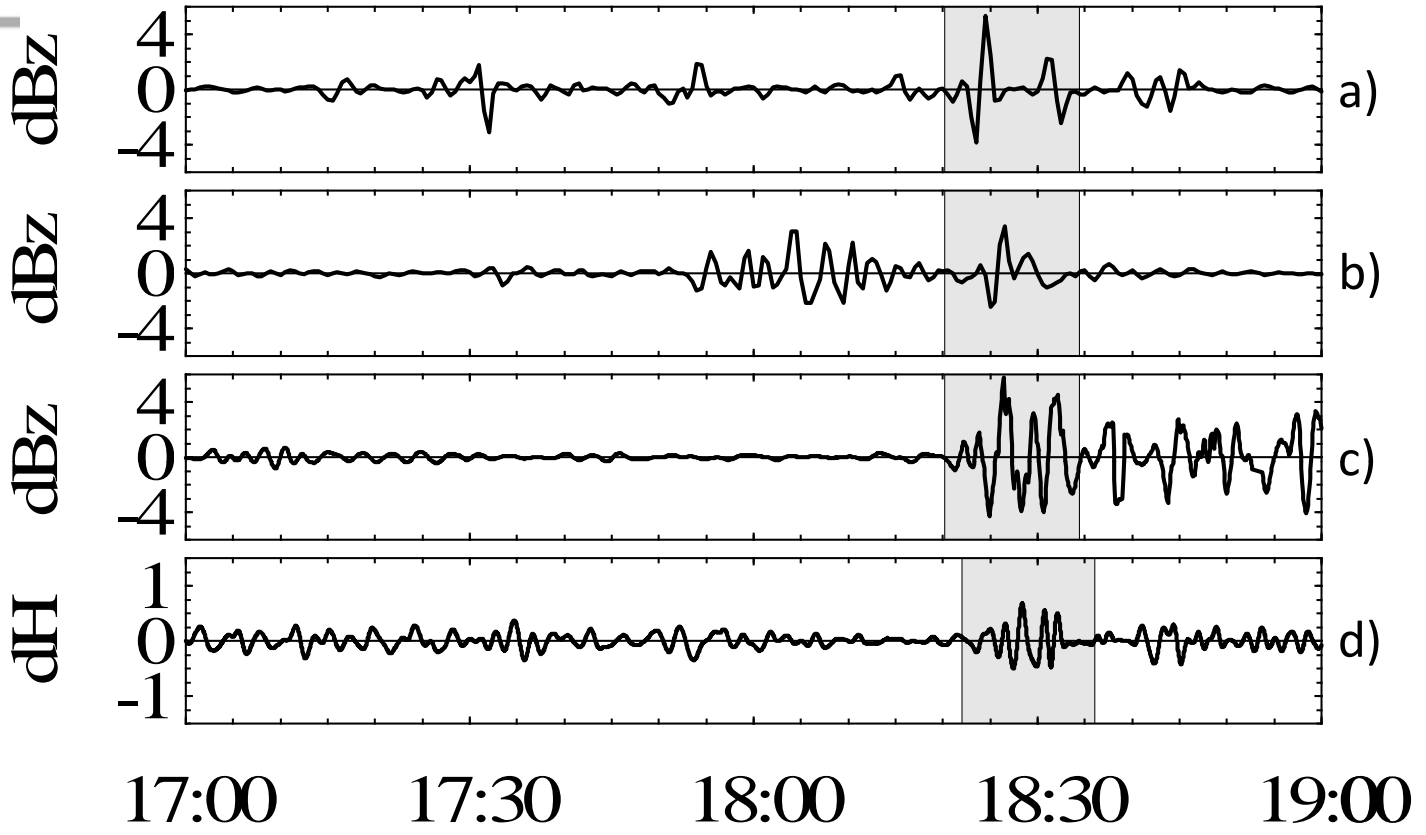


UCLA



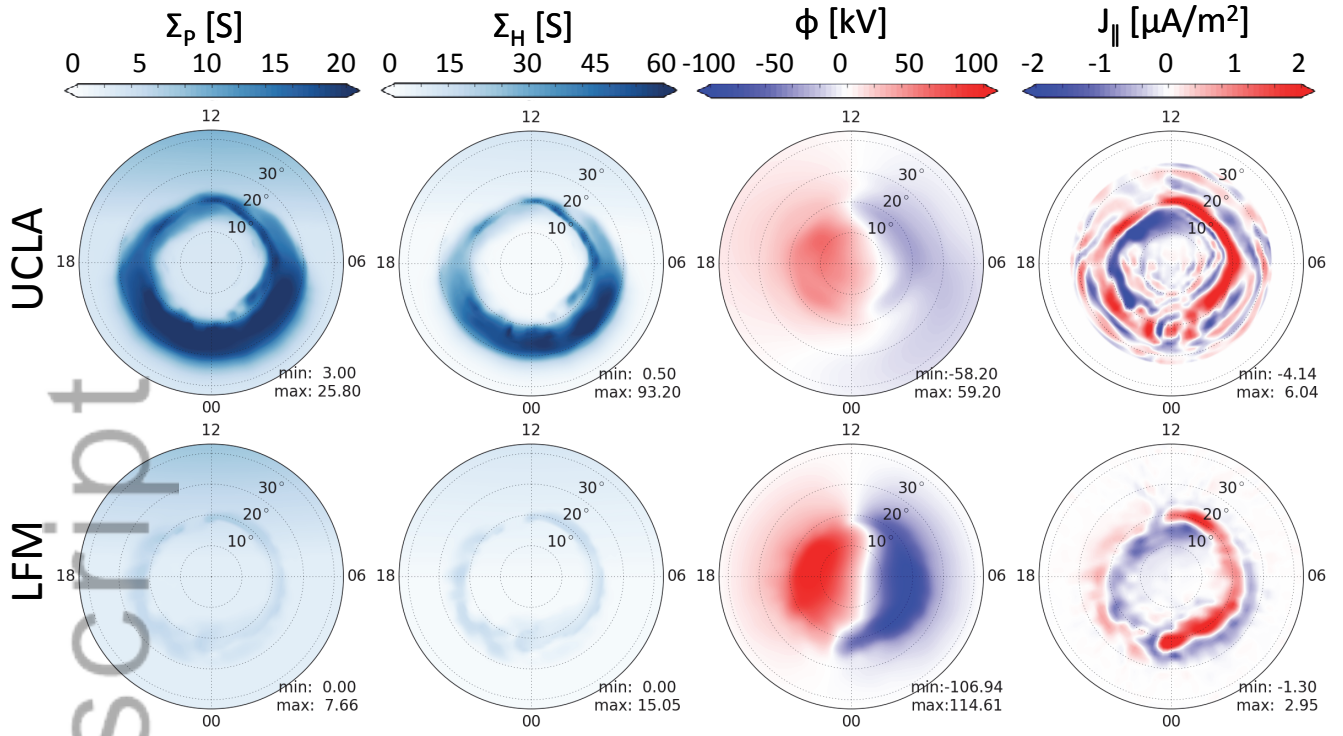
LFM





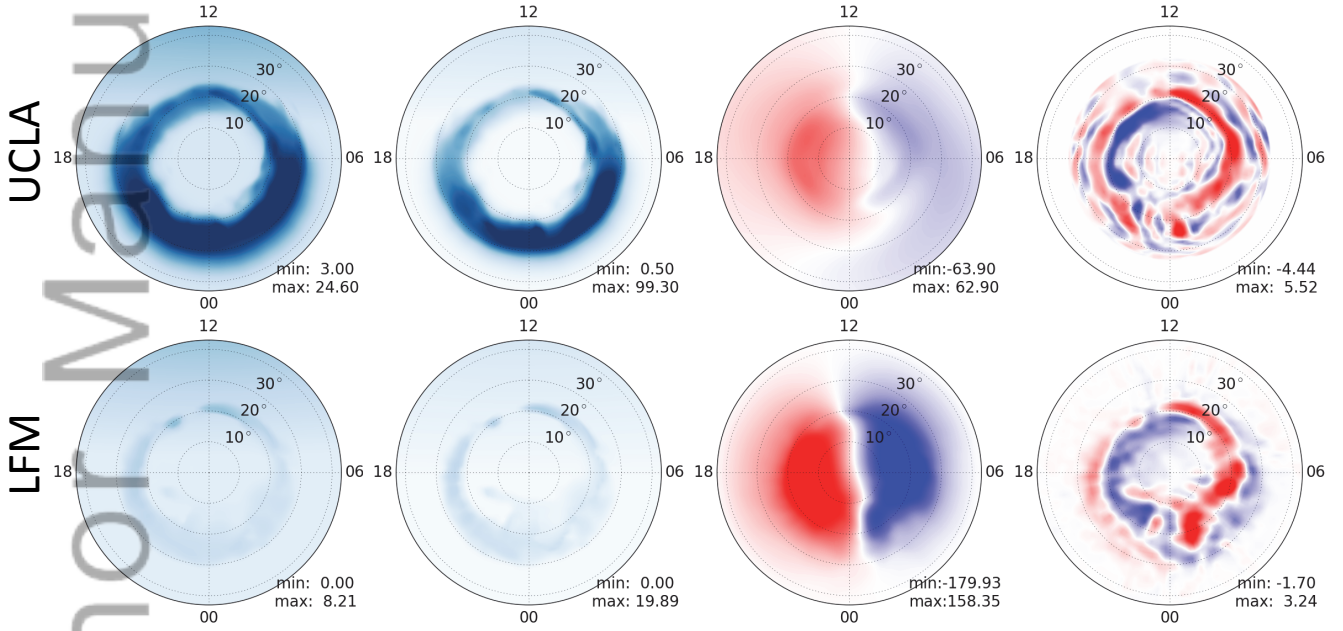
1808 UT

(pre-onset, disturbed interval)



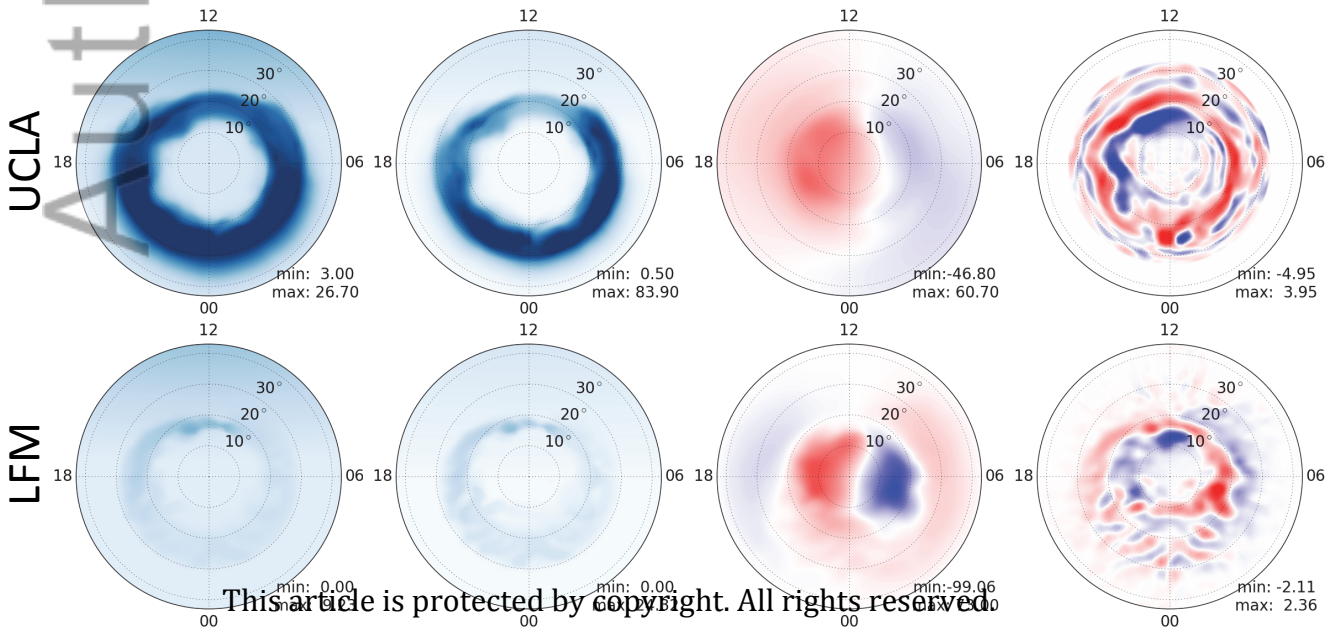
1828 UT

(onset/expansion phase)

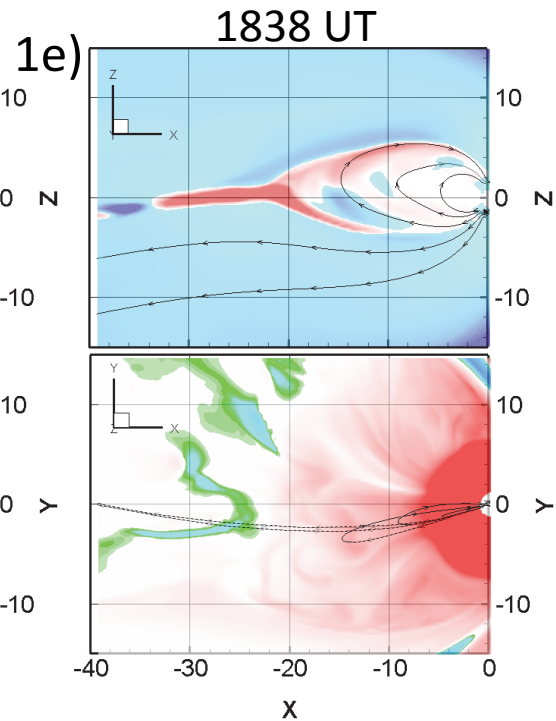
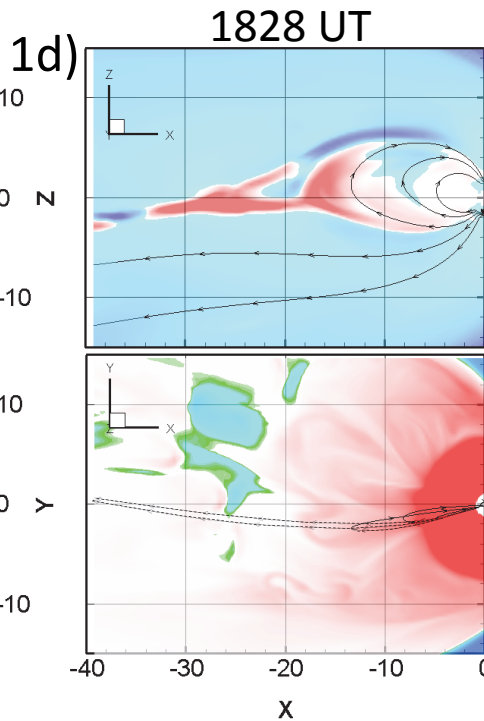
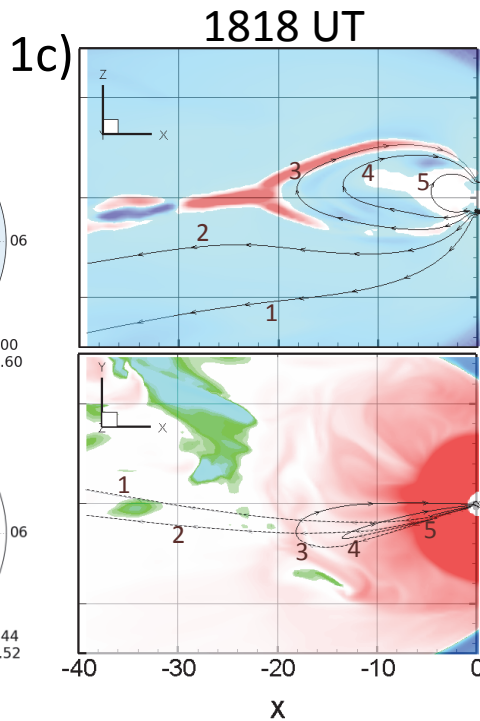
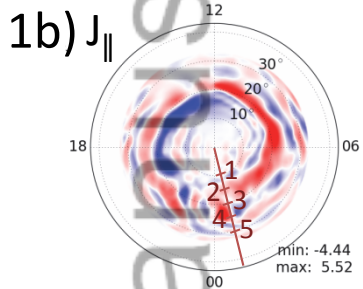
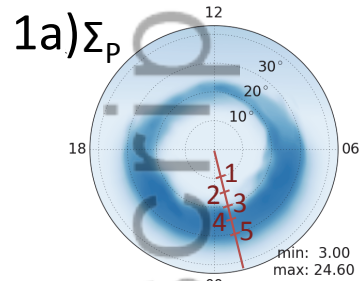


1848 UT

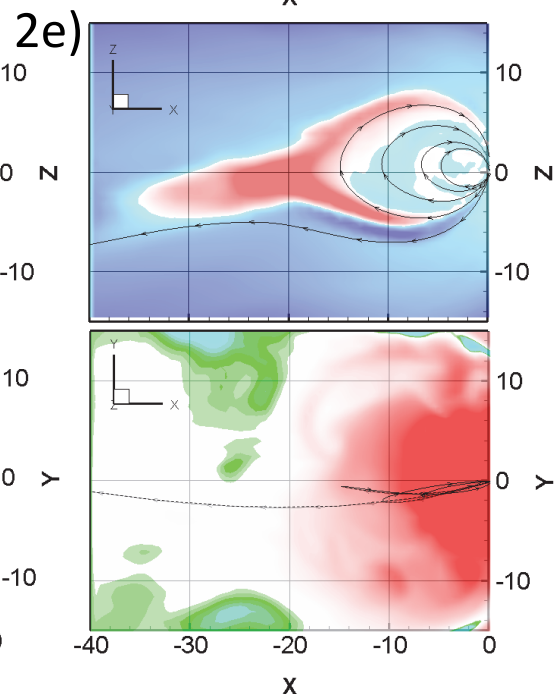
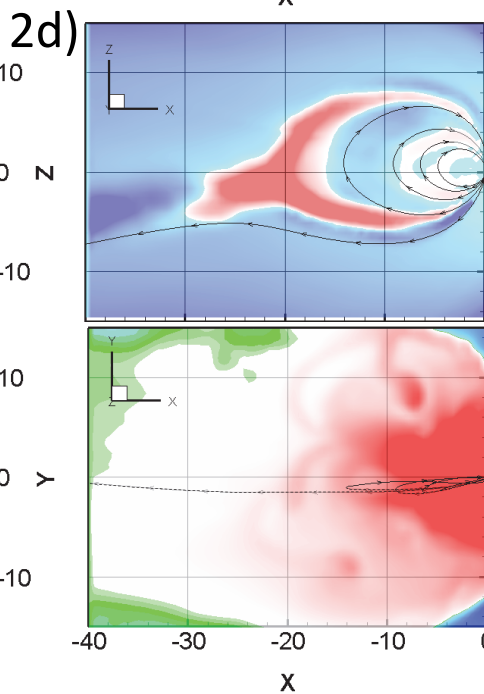
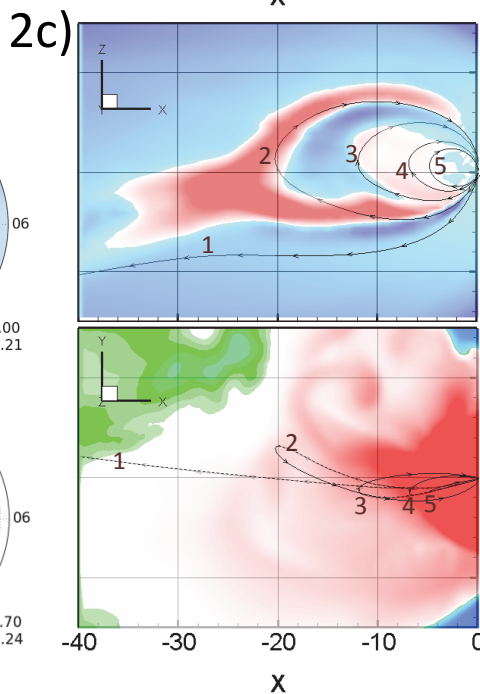
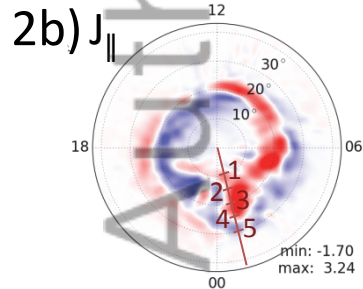
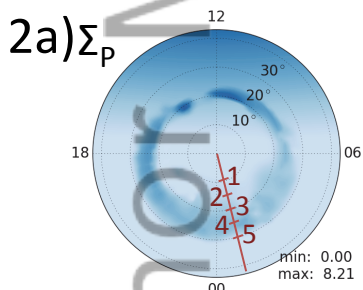
(recovery phase)

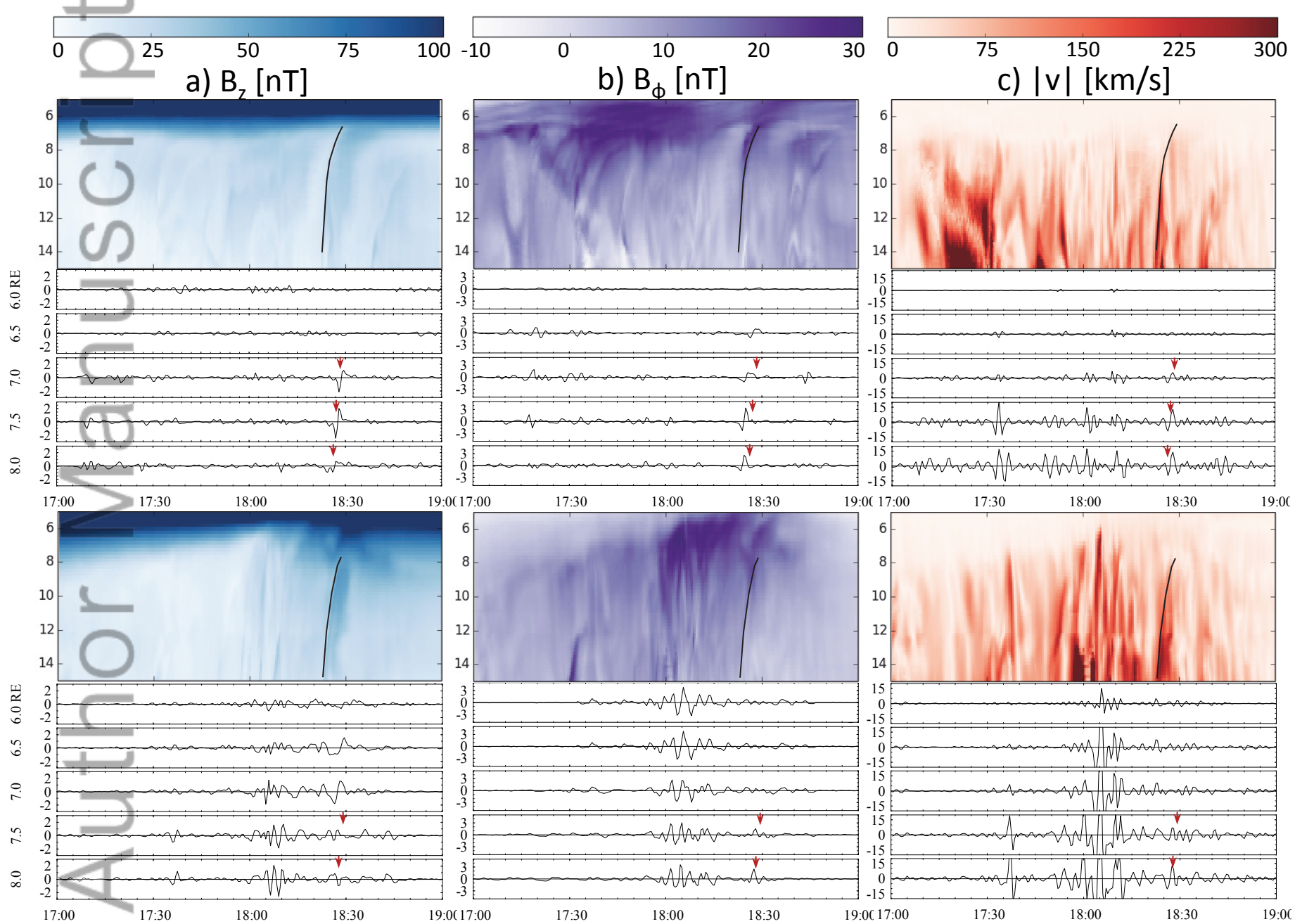


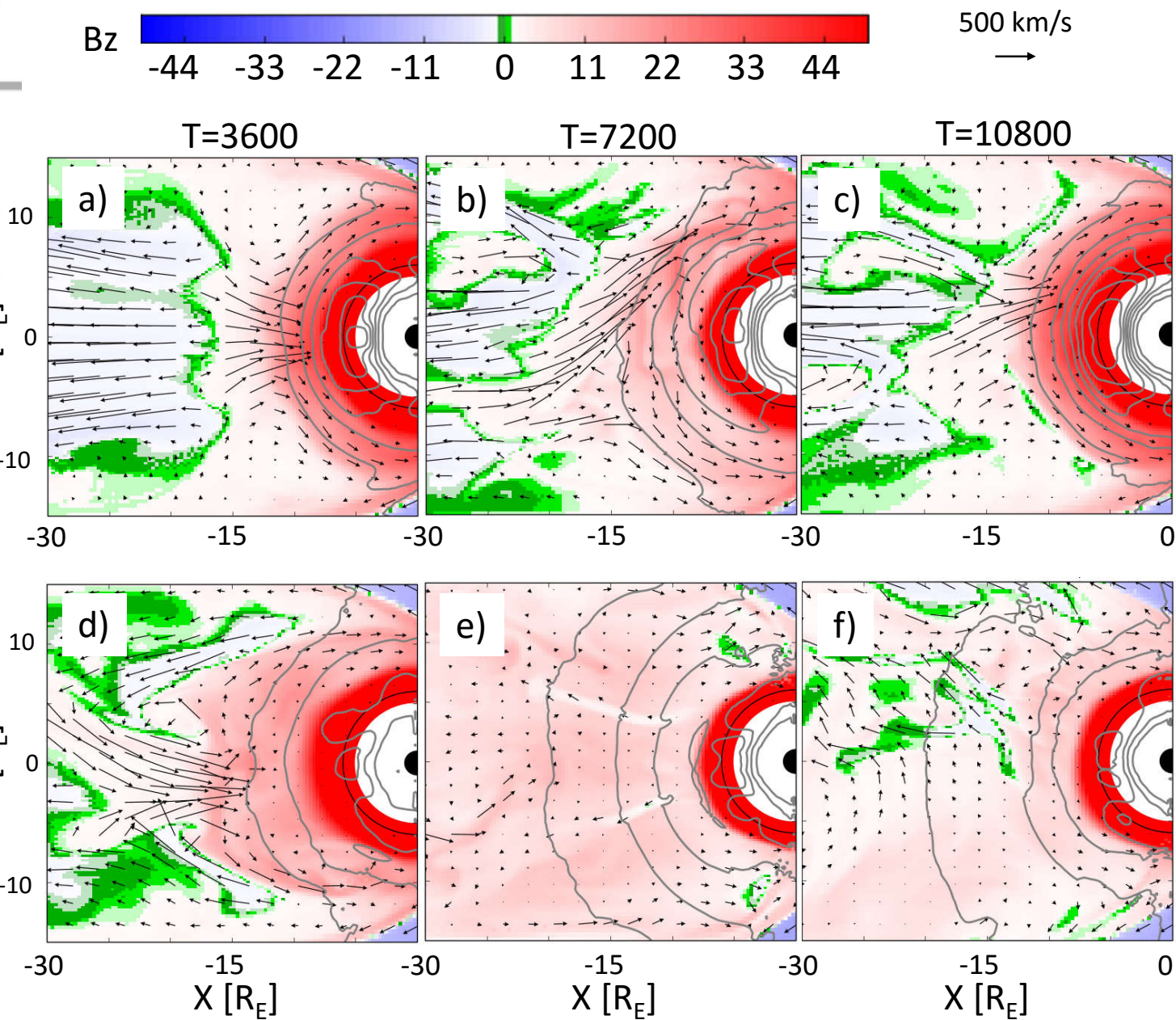
1) UCLA

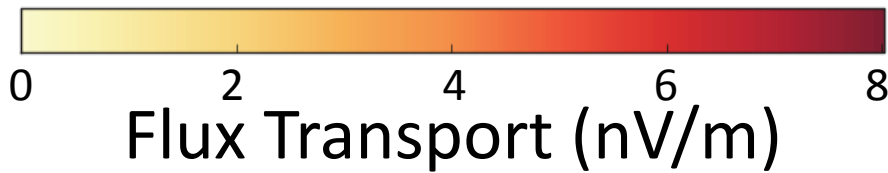


2) LFM

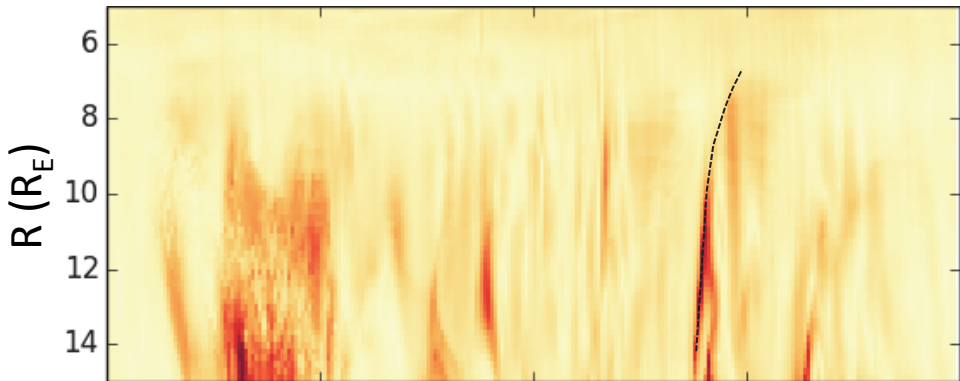








UCLA



LFM

